



# Comprehensive wave climate analysis of the Uruguayan coast

Rodrigo Alonso<sup>1</sup> · Sebastián Solari<sup>1</sup>

Received: 22 June 2020 / Accepted: 30 May 2021 / Published online: 16 June 2021  
© Springer-Verlag GmbH Germany, part of Springer Nature 2021

## Abstract

A detailed analysis of how the wave climate gradually varies from the Atlantic coast to the Río de la Plata (RDP) estuary coast of Uruguay is undertaken, exploiting a recently developed high-resolution wave hindcast. As a better knowledge and understanding of the wave climate along the coast is a valuable tool for coastal scientist and managers for analyzing and interpreting its dynamics, a comprehensive approach is taken in this work, exploring not only the behavior of integral wave parameters but also average wave spectra and wave systems obtained from spectra partitioning. Moreover, as the focus is made on coastal areas, the magnitude and direction of the wave energy flux are analyzed as well. It is found that the analysis of the wave climate sustains the division of the Uruguayan coast in three main regions, namely, Atlantic, Outer RDP, and Intermediate and Inner RDP. In the Atlantic coast, two swell systems and a wind sea system are identified, and spatial changes in the wave climate are driven mainly by changes on coastal orientation, where La Paloma was identified as a breaking point; in the RDP, swell systems strongly refracts and dissipates, resulting in a wave climate characterized by one to none swell systems and a wind sea system, with bathymetry and geometry of the estuary playing a major role in the spatial changes of the wave climate. The analysis allowed not only to identify several characteristics of each of the regions but also to better understand how different wave systems (sea and swells) explain these characteristics in the different regions.

**Keywords** Coastal waves · Wave climate · Spectral partitioning · Wave energy flux · Río de la Plata · South Atlantic Ocean · Long-term wave systems

## 1 Introduction

The Uruguayan coast is approximately 700 km long, from the mouth of the Uruguay and Paraná Rivers in the Río de la Plata Estuary (RDP) in the West to the border with Brazil in the Atlantic Ocean in the East (Fig. 1). Despite its heterogeneity, a common element is the presence of sandy beaches along the whole coast, whose dynamic is mainly driven by waves (Solari et al. 2018; Teixeira et al. 2012).

Previous works, focused on specific areas, evidenced that there are considerable differences in the wave climate along the Uruguayan coast. On one hand, the eastern part of the coast is open to the Atlantic Ocean, exposed to swells from different directions that frequently coexist which are reflected in a multimodal wave spectrum (see e.g., Pianca et al. 2010; Alonso et al. 2015; Romeu et al. 2015; Pereira et al. 2017). Atmospheric patterns behind these waves are mostly related to the South Atlantic Subtropical High (Sun et al. 2017) and the cyclogenesis over Southeastern South America (Gramcianinov et al. 2019). The latter is the main responsible for generation of extreme waves, and it was the object of recent studies of significant contribution to the understanding of the regional wave climate (Campos et al. 2018; Campos et al. 2019; Gramcianinov et al. 2020). On the other hand, the upper Río de la Plata Estuary has a wave climate that is dominated by short-fetched sea waves (see e.g., Dragani and Romero 2004). However, the unavailability of a high-resolution wave hindcast that properly incorporates sea level and current variation in the RDP has prevented the systematic and coherent study of the wave climate all along the Uruguayan coast. The recent development of a wave (and sea-level) hindcast of such characteristics (Alonso and Solari

---

This article is part of the Topical Collection on the *International Conference of Marine Science ICMS2018, the 3rd Latin American Symposium on Water Waves (LatWaves 2018), Medellín, Colombia, 19-23 November 2018 and the XVIII National Seminar on Marine Sciences and Technologies (SENALMAR), Barranquilla, Colombia 22-25 October 2019*

---

Responsible Editor: Alejandro Orfila

---

✉ Rodrigo Alonso  
ralonso@fing.edu.uy

<sup>1</sup> IMFIA – Universidad de la República, Julio Herrera y Reissig 565, 11300 Montevideo, Uruguay

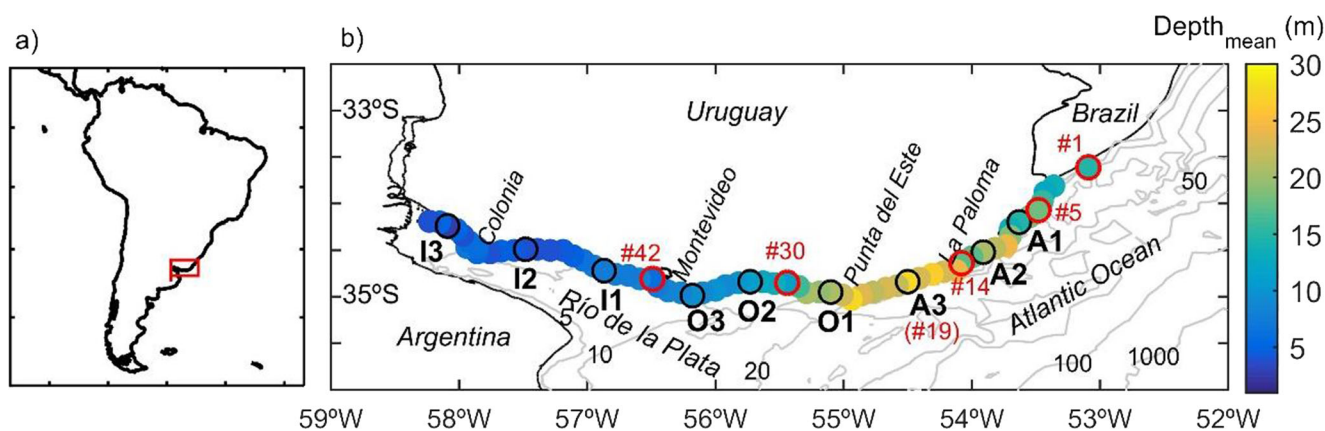


**Fig. 1** Study area: **a** location in the context of South America; **b** nodes of the wave hindcast used in this work. Since the wave hindcast considered non-stationary water levels, the mean depth is mapped. In bold are the nodes where detailed results are presented. “A” refers to the Atlantic (east

to Punta del Este), “O” to the Outer RDP (between Montevideo and Punta del Este), and “I” to the intermediate and inner RDP (west of Montevideo). General numbering begins at the easternmost node (# 1) and increases to the west. In red are the nodes used as an example in Fig. 2

2020) made it possible to undertake a detail analysis on how the wave climate gradually varies from the Atlantic coast to the RDP coast. To the best of our knowledge, this is the first detailed wave climate characterization of the Uruguayan coast and, as such, a significant contribution to the understanding and management of the coast in the region.

A better knowledge and understanding of the wave climate along the coast is a valuable tool for analyzing and interpreting its dynamics, as it is for coastal management in general. More traditional wave climate characterizations are based on integral wave parameters, as significant wave height ( $H_s$ ), mean period ( $T_{m01}$ ), and mean direction ( $D_m$ ). However, in recent years other approaches took advantage of the availability of spectral data in order to provide a more complete description of the wave climate, looking either at average spectra (Shimura and Mori 2019) or at its partitions (Portilla-Yandún et al. 2015). In addition to expanding and enriching the information provided, this kind of approaches become even more important when multimodal sea states are frequent, as is the case of the Uruguayan Atlantic coast. In these conditions, integral parameters, such as mean period and mean direction, start to significantly lose their meaning (Portilla-Yandún et al. 2019).

In this work, all the three approaches are explored and, in some cases, expanded. In particular, as the focus of the work is in coastal areas, the magnitude and direction of the wave energy flux (WEF) is analyzed along with the usual integral parameters, as they provide a better idea on how the wave climate would affect the coastal morphology (see e.g., Elshinnawy et al. 2017; Menstachi et al. 2017; Almar et al. 2015; Splinter et al. 2012; Chowdhury and Ranjan 2017).

The remainder of the paper is organized as follows. Materials and methods are introduced in Section 2: the used datasets are presented in Section 2.1; wave parameters and sample statistics that are used all along the work are defined in Section 2.2; lastly, Section 2.3 describes methodology used

for wave partition and for determining long-term wave systems (LTWS). Obtained results are presented in Section 3, which is organized in three parts: Section 3.1 presents the wave climate in terms of integral parameters; in Section 3.2, the average spectra are presented; and Section 3.3 shows results related with the wave systems. Then, a joint discussion is presented in Section 4 and conclusions are outlined in Section 5.

## 2 Materials and methods

### 2.1 Data

The wave spectra time series analyzed in this work are a product of the latest wave hindcast for Uruguayan waters (Alonso and Solari 2020). This hindcast was developed using the third-generation wave model WAVEWATCH III® version 5.16 (WWDG 2016) configured with the ST4 parametrization (Ardhuin et al. 2009). This choice of ST4 was based on its good performance in the western part of the South Atlantic Ocean reported in Stopa et al. (2016), Pereira et al. (2017), and Campos et al. (2018). The model employs five computational grids that exchange information with each other following the mosaic multi-grid two-way nesting approach (Tolman 2008), starting with a coarse global grid and reaching the Uruguayan coast and the intermediate and inner Río de la Plata with a 40'' spatial resolution (~1km). The wind forcing data comes from the CFSR atmospheric reanalysis (Saha et al. 2010) and its extension CFSv2 (Saha et al. 2014), and it was previously validated for the study area by a comparison against altimetry and in-situ wind velocity measures; even though it has been pointed out that these wind data base show temporary inconsistencies (Chawla et al. 2013) and might underestimate extremes (Campos et al. 2018; Campos et al. 2019) in the South Atlantic, Alonso and Solari (2020) showed their suitability for

the generation of a wave hindcast in the Uruguayan coast. The other forcings, non-stationary water levels and currents, were obtained from hydrodynamic simulations using the TELEMAC 2D model (Hervouet 2007). Regarding to bathymetry, the high-resolution bathymetry was generated from the local nautical charts provided by the hydrographic service of the Uruguayan Navy and complemented with the global ETOPO1 (Amante and Eakins 2009) where required. In Alonso and Solari (2020), the wave hindcast was calibrated and validated using the multi-mission altimetry database from Queffelec and Croizé-Fillon (2013) along with in situ measurements at seven nearshore points, showing the good performance of the hindcast in the study area.

Figure 1 b shows the location of the 65 nodes of the wave hindcast considered for this work. They are uniformly distributed along the coast, at about 5 km from the coast and about 10 km between each other. It is observed that despite maintaining an almost constant distance from the coast, the depth at the nodes is variable. In the Atlantic coast, it varies in the range of 20–30 m between Punta del Este and La Paloma, and in the range of 15–25 m to the east of La Paloma. On the other hand, in the RDP, it decreases from 25 to 2.5 m, following the bathymetry trend of the estuary. Throughout the article, detailed results are presented for the nine nodes highlighted on Fig. 1b: three of them correspond to the Atlantic coast (A1, A2, and A3); three are in the outer RDP (O1, O2, and O3); and three in the intermediate and inner RDP (I1, I2, and I3). Their location and average depth are shown in Table 1.

The wave spectra time series span the 1985–2016 period with 1 h time step. The spectra are discretized in 36 uniformly distributed directions and 25 frequencies starting at 0.0418 Hz and increasing exponentially with factor 1.1 (i.e.  $f_{i+1} = 1.1f_i$ ). The high resolution of the hindcast, as well as its validation against in-situ near-shore measurements, brings confidence to the data base, particularly for its use in climatological analysis that focus on average conditions, as is the case here.

The wind data used to separate wind sea from swells and to identify the generation zones of swells were the same that force the wave hindcast (NCEP CFSR and CFSv2; Saha et al. 2010, Saha et al. 2014).

Some climate indexes were used to analyze to what extent the wave climate variability in the study area can be related to the patterns of recognized influence on the region. One is the Antarctic Oscillation Index (AAO), defined by Gong and Wang (1999). It is an indicator of the Southern Annular Mode, which is the dominant pattern of large-scale atmospheric variability in the extratropical Southern Hemisphere (Marshall 2003). The other climate index considered is the Southern Oscillation Index (SOI) defined by Walker and Bliss (1932 and 1937). It is an indicator of El Niño Southern Oscillation (ENSO) whose associated effects occur all over the world (Collins et al. 2010), including the southern

Atlantic (e.g., Pisciotto et al. 1994; Rodrigues et al. 2015; Martín-Gómez et al. 2020). Monthly values of AAO index and SOI for the period 1985–2016 were obtained from the Physical Science Laboratory of NOAA<sup>1</sup>

## 2.2 Wave parameters and sample statistics

### 2.2.1 Wave parameters

The parameters used to summarize spectral information are significant wave height ( $H_s$ ), mean period  $T_{m01}$ , mean direction ( $D_m$ ), peak period ( $T_p$ ), peak direction ( $D_p$ ), and wave energy flux (WEF). They are calculated by integrating the spectral energy density ( $S(f, \theta)$ ) as follows:

$$H_s = 4.004 \times \sqrt{\int_0^{2\pi} \int_0^\infty S(f, \theta) df d\theta} \quad (1)$$

$$T_{m01} = \left[ \int_0^{2\pi} \int_0^\infty S(f, \theta) df d\theta \right] / \left[ \int_0^{2\pi} \int_0^\infty S(f, \theta) f df d\theta \right] \quad (2)$$

$$D_m = \tan^{-1} \left( \frac{b}{a} \right),$$

$$\text{with } a = \int_0^{2\pi} \int_0^\infty \cos(\theta) S(f, \theta) df d\theta \quad \text{and } b = \int_0^{2\pi} \int_0^\infty \sin(\theta) S(f, \theta) df d\theta; \quad (3)$$

Spline interpolation was used to provide a more precise estimation of the peak parameters  $T_p$  and  $D_p$ . Regarding to WEF, its magnitude ( $\|WEF\|$ ) and direction ( $\theta_{WEF}$ ) were calculated as follows:

$$\|WEF\| = \sqrt{WEF_x^2 + WEF_y^2}, \quad \theta_{WEF} = \tan^{-1} \left( \frac{WEF_y}{WEF_x} \right), \quad (\text{with})$$

$$WEF_x = \int_0^{2\pi} \int_0^\infty \cos(\theta) S(f, \theta) \cdot C_g(f, h) df d\theta \quad \text{and}$$

$$WEF_y = \int_0^{2\pi} \int_0^\infty \sin(\theta) S(f, \theta) \cdot C_g(f, h) df d\theta; \quad (4)$$

with  $C_g$  as the group velocity calculated from frequency ( $f$ ) and water depth ( $h$ ) using linear wave theory.

Average wave parameters ( $H_s^{as}$ ,  $T_{m01}^{as}$ , and  $D_m^{as}$ ) were also estimated by means of Eqs. 1, 2, and 3 but using the average 2D spectrum  $S^{as}(f, \theta)$ , which is composed of the time-averaged energy of each spectral bin (see Shimura and Mori 2019). For the peak parameters of the average spectrum, the peak parameters of the 2D average spectrum ( $T_p^{as}$  and  $D_p^{as}$ ) were distinguished from the peak of the 1D average frequency spectrum ( $T_p^{afs}$ ) and the peak of the 1D average directional spectrum ( $D_p^{ads}$ ).

<sup>1</sup> <https://psl.noaa.gov/data/climateindices/list/> (last visited on March 31th 2020)

**Table 1** Location and mean depth at selected nodes where detailed results are presented

	A1	A2	A3	O1	O2	O3	I1	I2	I3
Coordinates	53.63W; 34.2S	53.91W; 34.52S	54.5W; 34.84S	55.1W; 34.95S	55.73W; 34.84S	56.18W; 34.99S	56.87W; 34.72S	57.48W; 34.49S	58.09W; 34.24S
Mean Depth (m)	14.8	20.9	27.6	20.6	11	9.5	7.7	4	2.7

### 2.2.2 Sample statistics

Mean and standard deviation are used to report central tendency and dispersion of the data and the 99th percentile is used as a reference value for extremes. In the case of directions, the median ( $Dm_{50}$ ) and the interquartile range (difference between the 75th and 25th percentile;  $Dm_{75-25}$ ) are used instead of the mean and the standard deviation, while the difference between the 99th and 1st percentile ( $Dm_{99-1}$ ) provides a reference of the amplitude of the complete arc from which the waves arrive. In some cases, coefficient of variation (COV), defined as the mean over the standard deviation, is used to present dispersion of the data instead of the standard deviation. COV was also estimated in annual scale to analyze inter-annual variability, calculated from the time series of annual mean values. In the case of directions, the inter-annual variability was measured as the interquartile range estimated from the time series of annual median values (annual  $Dm_{75-25}$ ).

Regarding the correlations performed, it is necessary to provide some details. The maximum correlation ( $Corr_{max}$ ) is defined as the maximum absolute value of the linear correlation that is obtained between two time series by varying the time lag between them. This statistic is used to measure (a) the correlation between  $H_s$  of swell systems at the node A1 and the wind speed at several locations, projected on the great circle that links each location with the node A1 (following Jiang and Mu 2019), and (b) to estimate correlation between wave systems at different locations. Finally, monthly series were used to correlate with climate indexes. This series were obtained averaging over time to have monthly means and averaging in space in regions with high spatial correlation. Therefore, these are series of monthly averages of  $H_s$  by wave systems, representative of areas where the system presents a strong spatial correlation.

### 2.3 Identification of wave systems

Wave spectra time series were used to identify several long-term wave systems (LTWS), which are groups of individual wave systems that have a similar origin (Portilla-Yandún et al. 2019). For each location, a wind sea long-term system and one or two swell long-term systems were identified. To this end, the next steps were followed: (i) partition of each spectra to separate individual wave systems; (ii) identification of spectral

partitions (i.e., individual wave systems) corresponding to wind seas and swells; (iii) determination of the LTWS at each node; and (iv) regroup some of the LTWS to avoid discontinuities in the characterization of LTWS in adjacent locations. While step (iii) follows Portilla-Yandún et al. (2015), whose methodology was originally proposed for deep waters, step (iv) was required in this case to adapt the methodology for the behavior observed in shallow waters.

For spectral partition, the methodology used in WAVEWATCH III® (WW3DG 2019) is followed: the spectral surface is inverted, and based on the analogy with a topographic surface, the spectral peaks become catchment and the watershed lines define the partition boundaries. To determine watershed lines, the algorithm available in MATLAB® image processing toolbox (Meyer 1994) was used. Then, the partitions whose  $H_s$  are less than 0.25 m were discarded to reduce noise in the posterior T-D bivariate distribution.

Wind seas were identified using the wave age criterion proposed by Hanson and Phillips (2001),

$$C_p \leq 1.5 U_{wind} \cos \delta, \quad (5)$$

where  $C_p$  is the phase velocity of the waves calculated from the peak period of the wave partition and the water depth,  $U_{wind}$  is the 10 m elevation wind velocity, and  $\delta$  is the angle between the wind and the peak direction of the wave partition. The spatial resolution of CFSR reanalysis is often not sufficient to properly represent wind changes on sea-land transition, usually leading to an underestimation of wind velocity in the nearshore. To avoid this affecting the Hanson and Phillips criterion,  $U_{wind}$  was estimated at each location from its closest CFSR node that is completely on water (i.e., a node on water whose neighboring nodes are also on water). Further corrections were necessary to also take into account potential refraction of the wind sea in the continental shelf. As refraction in the nearshore can deviate direction of the wind sea from that of the wind, increasing  $\delta$  and therefore decreasing the right hand side term of [5] causing a wave partition not to be classified as wind sea when in fact it is. To address this issue, the following criteria was adopted for conditions with  $U_{10}$  higher than 2 m/s blowing from the sea: if a wave partition is classified as wind sea by wave age criterion [5], no further correction is made; if no partition is classified as wind sea by wave age criterion [5] but the wave direction of the partition is closer to the perpendicular to the coast than the wind direction, then



wave age criterion [5] is revisited but imposing  $\delta=0$ ; lastly, if more than one individual wave partition is classified as wind sea, only the one with the larger steepness is considered and the other(s) is(are) classified as swell.

Then, long-term swell systems were determined at each node following Portilla-Yandún et al. (2015) and considering only those partitions classified as swell. This technique involves a new round of partitioning, but this time applied to the T-D bivariate distribution of partitions classified as swell (see Fig. 2), based on the idea that similar generation patterns leading to swells with similar periods and directions.

Several nodes in the Atlantic and part of the outer RDP coast present two clearly differentiated LTWS (see Fig. 2a and b); these were named eastern swells (singled out in cyan in Fig. 2) and southern swells (singled out in red), according to their main directions. However, for some nodes, these systems split in more than two LTWS; in these cases, the LTWS were grouped to rebuild the Eastern and Southern swell systems (see Fig. 2c and d), according to the following criteria: if the peak of the LTWS is between the perpendicular to the coast and the SW, it was assigned to the Southern swell system, while it was assigned to the Eastern swell system if it is between the perpendicular to the coast and the NE. In this way, swells were grouped in two systems along the entire Atlantic coast and part of the outer RDP (Southern and Eastern swells), up to a point where both systems merged, and it was not possible to differentiate them. From that point, all swells are approximately aligned to the SE and were grouped into a single system named RDP swells (singled out in yellow in Fig. 2e and f). Lastly, there were some systems corresponding to wave partitions that even though they were not identified as wind seas, they can hardly be associated with swell conditions; these systems (singled out in black in Fig. 2) are associated with partitions coming from fetch limited directions that remain after a change of wind direction. Consequently, these systems are relabeled as wind seas.

### 3 Results

Results are presented and briefly discussed in this section, differentiating among those resulting from the analysis of integral wave parameters (Section 3.1; Figs. 3, 4, 5, 6, 7, 8, 9, 10, 11, and 12), average spectra (Section 3.2; Figs. 13, 14, 15, 16, and 17), and long-term wave systems (Section 3.3; Figs. 18, 19, 20, 21, 22, 23, 24, 25, 26, 27, 28, 29, 30, and 31). A joint discussion of all results is presented afterwards, in Section 4.

#### 3.1 Integral parameters

The spatial distribution of the sample statistics used to measure central tendency, dispersion, and extreme values

can be seen in Figs. 3, 4, and 5. Figures 3 and 4 contain maps of the mean, COV and 99th percentile of  $H_s$ , and  $T_{m01}$ , respectively. Figure 5 presents maps for  $D_m$ , with the median, the interquartile range, and the difference between 99th and 1st percentiles.

As expected, because it is open to the ocean and therefore not limited by fetch, the Atlantic coast (east of Punta del Este) is exposed to a more energetic wave climate than the Río de la Plata coast. Figure 3a shows how mean  $H_s$  varies between 1.3 and 1.7 m in the Atlantic and then gradually decrease into the Río de la Plata, reaching values less than 0.5 m in most of the intermediate and inner RDP nodes (west to Montevideo). The other spatial pattern to note is the change around La Paloma, accompanying the change in the orientation of the coast; mean  $H_s$  around 1.55 m is observed in nodes east of La Paloma and around 1.4 m in nodes that are to the west and still in the Atlantic.

In Fig. 3b, it is shown that  $H_s$  COV presents a spatial pattern opposite to that of mean  $H_s$ ; i.e., the lower values are in the Atlantic and there is a gradual increase of  $H_s$  COV from the outer to the inner Río de la Plata. On the other hand, Fig. 3c shows that the spatial pattern of  $H_s$  99th is similar with that of the mean but with a smaller amplitude of relative variation. While  $H_s$  mean in the Atlantic is 10 times greater than  $H_s$  mean in the innermost node of the Río de la Plata, if  $H_s$  99th is compared, this ratio decreases to around 3.5.

In Fig. 4a, it is noted that spatial variation of mean  $T_{m01}$  shows a sharp change around Montevideo. Mean  $T_{m01}$  is larger than 6 s in the nodes of the outer RDP (east to Montevideo) and the Atlantic, and lower than 5 s in the nodes of the intermediate and inner RDP (from Montevideo to the west) as this zone is less exposed to swells. Regarding variability of  $T_{m01}$ , Fig. 4b shows that, as was observed for  $H_s$ ,  $T_{m01}$  COV increases into the estuary.

From Fig. 5a and b, it follows that, along the entire coast,  $D_m$  of most of the sea states are included in the SE quadrant (E to S). It is also observed in Fig. 5b that, contrary to  $H_s$  and  $T_{m01}$ ,  $D_m$  presents more variability in the Atlantic than in the Río de la Plata.

The intra-annual variability of  $H_s$ ,  $T_{m01}$ , and  $D_m$  is presented in Fig. 6 through their corresponding annual cycles at the nine selected nodes (see Fig. 1b). For  $H_s$  and  $T_{m01}$ , monthly averages are considered, while for  $D_m$ , the monthly median is used.

From Fig. 6e and f, it follows that variability in wave directions is mostly related with its annual cycle; its range in the Atlantic is approx.  $30^\circ$ , with a clockwise rotation (more southern waves) during cold seasons (AMJ and JAS) and counter-clockwise rotation (more eastern waves) during warm seasons (OND and JFM); this same pattern is also observed in the RDP but with smaller amplitude.

The annual cycles of  $T_{m01}$  (Fig. 6c and d) present a similar shape for all nodes, with larger (smaller) periods during cold

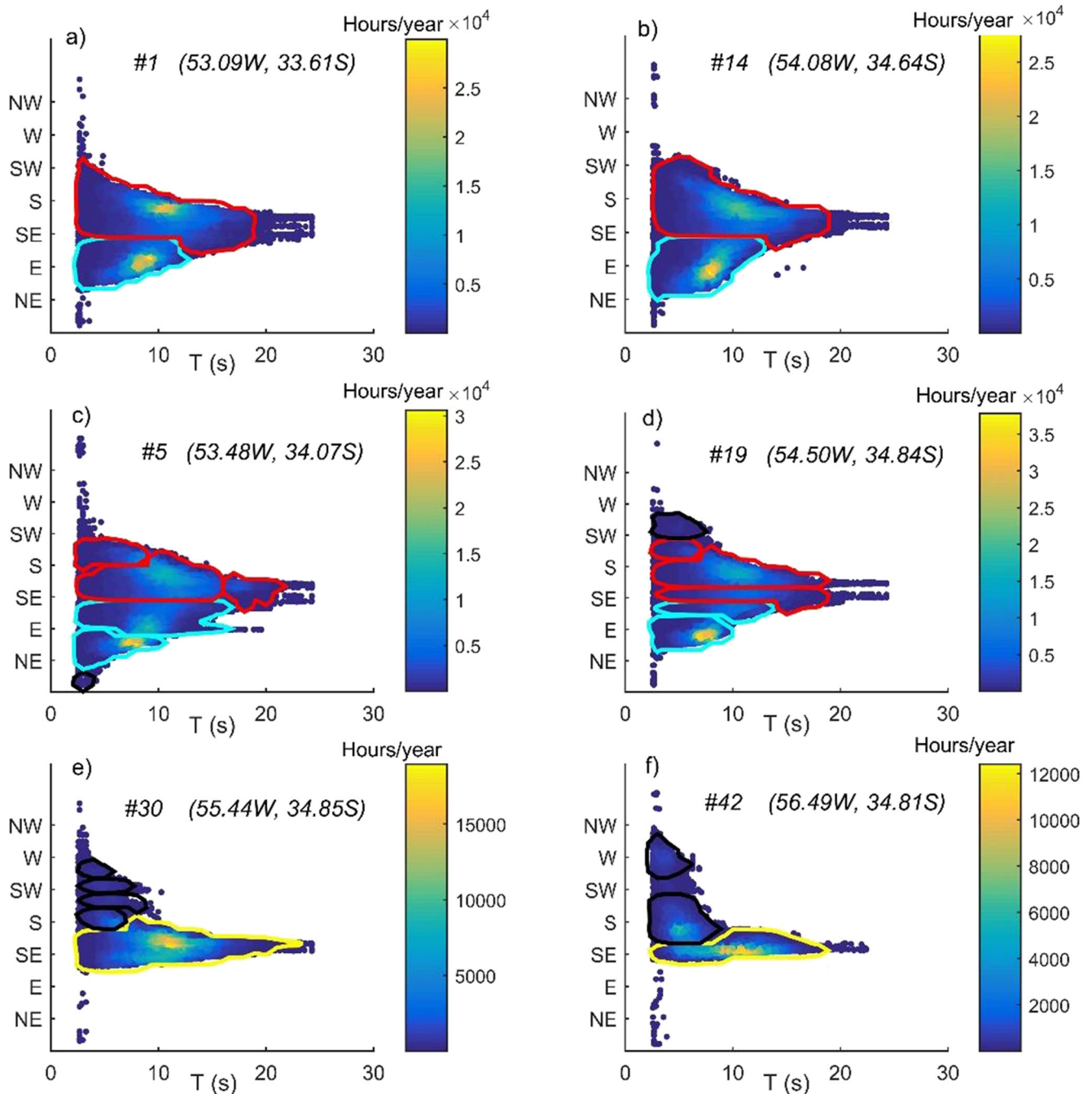


**Fig. 2** Examples of delimitation of Southern swell system (in red), Eastern swell system (in cyan), and RDP swell system (in yellow) based on partitioning the  $T_p$ - $D_p$  bivariate distribution of swells

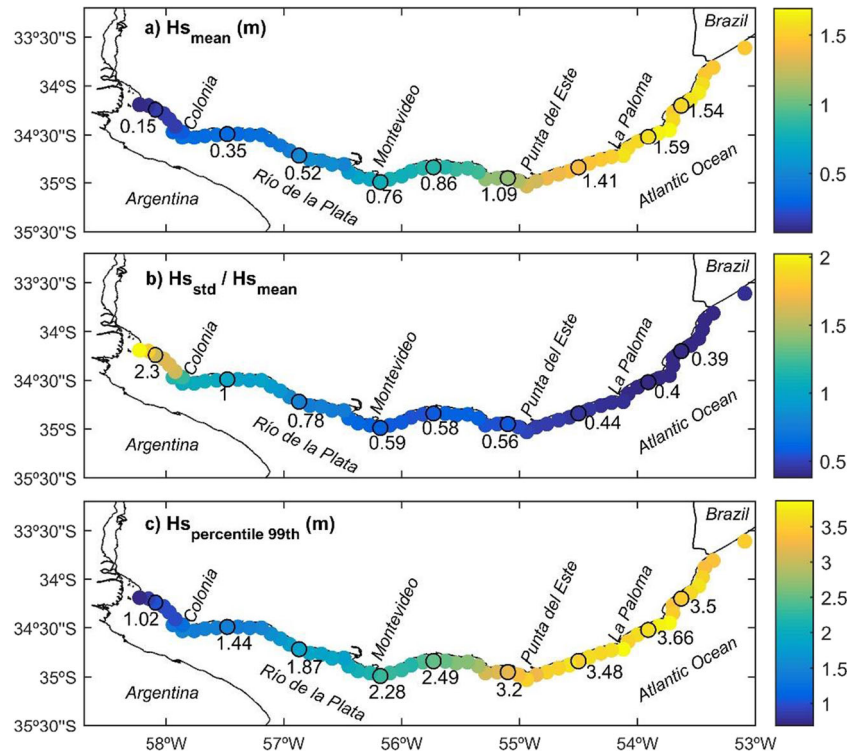
(warm) seasons, while the annual cycles of  $H_s$  (Fig. 6a and b) show some differences among the different nodes but all show a spike in September; the main difference is observed in autumn (AMJ): the inner RDP nodes show values lower than the mean (Fig. 6b), while the outer RDP and Atlantic nodes show values larger than the mean (Fig. 6a).

The inter-annual variability of  $H_s$ ,  $T_{m01}$ , and  $D_m$  is presented in Figs. 7 and 8. Figure 7 presents the maps of the COV at annual scale for the three parameters (annual  $D_{m75-25}$  in the

case of  $D_m$ ), while Fig. 8 presents the time series of their annual mean (median in the case of  $D_m$ ) at the nine selected nodes.

It is observed in Fig. 7a that the variability of  $H_s$  on an annual scale maintains the spatial pattern observed for  $H_s$  COV (Fig. 3b) but with a smaller range.  $H_s$  COV<sub>annual</sub> is around 0.03 in the Atlantic and increases toward the inner Río de la Plata up to 0.1. Figure 7.b shows that the inter-annual variability of  $T_{m01}$  is lower than that of  $H_s$ ,

**Fig. 3** Spatial distribution of  $H_s$  statistics: **a** mean, **b** COV, and **c** 99th percentile



showing no significant variations along the coast with  $T_{m01}$   $COV_{annual}$  between 0.015 and 0.027. Regarding  $D_m$ , Fig. 7c shows that in the Atlantic difference, almost  $5^\circ$  are expected between different years, and that these differences decrease to less than  $1^\circ$  in the intermediate

and inner RDP. Figure 8 shows how the variability represented by  $COV_{annual}$  is expressed in the time domain, standing out a cycle of almost 20 years which is more clearly seen for  $T_{m01}$  at the Atlantic and Outer RDP nodes (Fig. 8c).

**Fig. 4** Spatial distribution of  $T_{m01}$  statistics: **a** mean, **b** COV, and **c** 99th percentile

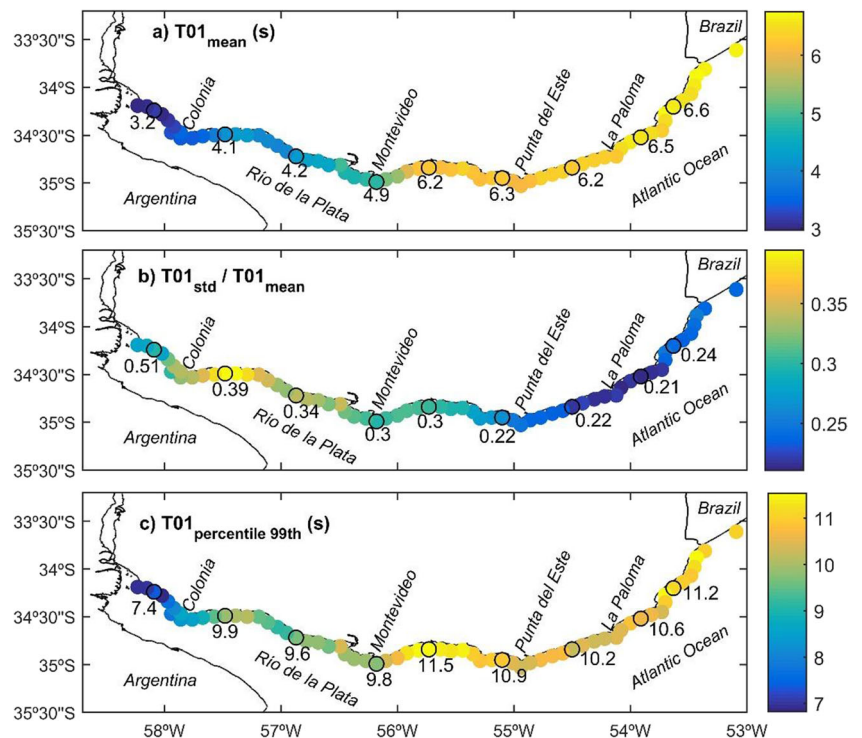
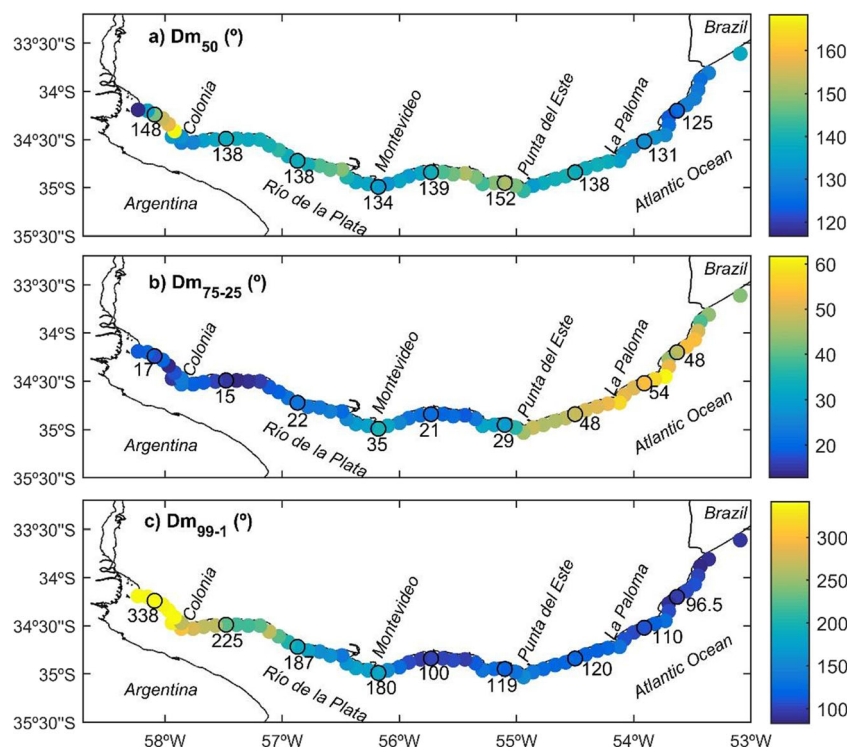


**Fig. 5** Spatial distribution of  $D_m$  statistics: **a** median, **b** difference between 75th and 25th percentile, and **c** difference between 99th and 1st percentile



Results regarding the wave energy flux are presented in Figs. 9, 10, 11, and 12. Figure 9 shows maps with the mean magnitude and median direction of the WEF, while Fig. 10 presents their annual cycle, and Figs. 11 and 12 present inter-annual variability results.

Figure 9a shows how wave energy is distributed along the coast. A similar spatial pattern to that of  $H_s$  is observed, but with stronger gradients: there is 10 kW/m east of La Paloma, which falls to 8 kW/m to its west, up to the Río de la Plata; once in the outer RDP, it strongly decreases to 1.7 kW/m near to Montevideo, and then it continues decreasing in the I&I RDP up to extremely low values in the innermost part of the estuary. Regarding WEF directions (Fig. 9b), they present an approx. 5° clockwise rotation from  $D_{m50}$  (Fig. 5a) along the entire coast, which indicates that the waves from the south are on average more energetic than those from the east.

Figure 10a shows that from April to September, in the Atlantic and in the outer RDP, waves are more energetic than the mean, with a spike in September. This September spike is also observed in the I&I RDP (Fig. 10b); however, from April to July, waves in this zone are less energetic than the mean. In terms of WEF direction (Fig. 10c and d), it is observed that for the entire coast, it tends to rotate towards the south from April to August, with its southernmost position occurring in June (with a more pronounced peak in the I&I RDP), while in the rest of the year, it rotates towards the east.

Figure 12 shows inter-annual variability of WEF; what stands out is the positive trend (southward rotation) of WEF direction for the entire coast (Fig. 12c and d).

### 3.2 Average spectra

Figure 13 shows average spectra for three of the selected nodes, one from the Atlantic (A2), one from the outer RDP (O2), and one from the intermediate and inner RDP (I2). In all cases, the two-dimensional average spectrum (central panels) is accompanied by two one-dimensional average spectra, one integrated into directions that presents the average energy distributed in frequencies (left panels), and the other integrated into frequencies presenting the average energy distributed in directions (right panels). All spectra are complemented with the values of integral and peak parameters obtained from them, i.e.,  $T_p^{afs}$ ,  $H_{m0}^{as}$ ,  $T_{m01}^{as}$ ,  $D_m^{as}$ ,  $T_p^{as}$ ,  $D_p^{as}$ ,  $D_{p1}^{ads}$ , and  $D_{p2}^{ads}$ . Also, average spectra at the selected nodes were normalized by their significant wave height and superimposed in Fig. 14.

Average wave spectra obtained in the Atlantic nodes were all bimodal (see Fig. 13b and c, and Fig. 14b), with one mode associated with the South and the other with the East. It is observed in Fig. 14b that the main difference between A3 (west of La Paloma, see Fig. 1) and A2 (east of La Paloma) is a reduction of the peak of A3 corresponding to the East mode. On the other hand, bimodality is no longer perceived in the RDP (Fig. 14b), where a single peak is observed around the SE direction (see Fig. 13e, f, g, and h, and Fig. 14b). Another difference between the Atlantic and the RDP is the larger relative weight of the SW quadrant (S to W). In terms of period, Fig. 14a shows that in the Atlantic and in O1 and O2, the peak of the spectra is located in periods associated with



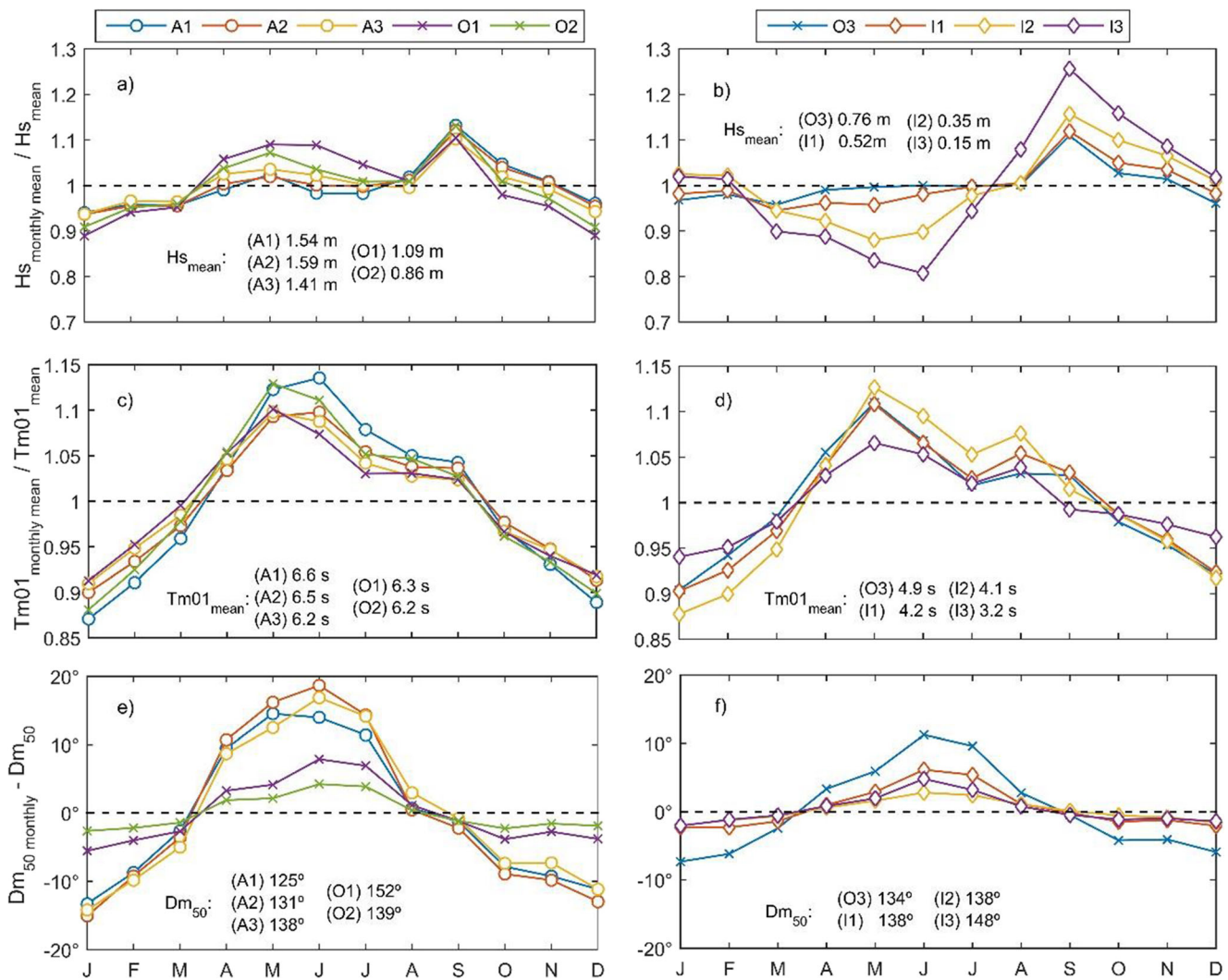


**Fig. 6** Annual cycles of **a** and **b**  $H_s$ , **c** and **d**  $T_{m01}$ , and **e** and **f**  $D_{m50}$  at nodes A1, A2, A3, O1, and O2 (left panels) and nodes O3, I1, I2, and I3 (right panels)

swells (i.e., ~10 s), and shifts to periods associated with wind seas (i.e., < 6 s) in O3 and in the nodes of the intermediate and inner RDP.

Intra-annual variations in terms of average spectrum are presented in Figs. 15, 16, and 17 for nodes A2, O2, and I2, respectively. Four seasons were considered: grouping January, February, and March (JFM) for summer; April, May, and June (AMJ) for autumn; July, August, and September (JAS) for winter; and October, November, and December (OND) for spring.

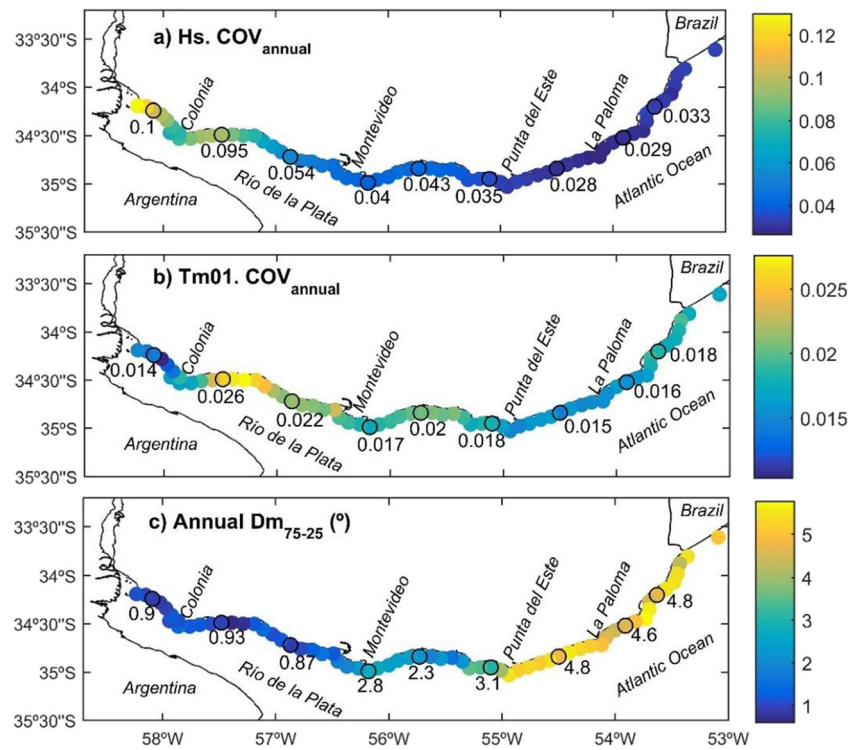
In the Atlantic, Fig. 15 shows that seasonal variability exhibits differences between the two modes. While the southern mode oscillates between a high level of energy during cold seasons (AMJ and JAS) and a lower one during warm seasons (OND and JFM), the eastern mode has more energy in spring (OND), less in autumn (AMJ), and intermediate levels in winter (JAS) and summer (JFM). Variations in the location of the peak period of the seasonal average spectra are also observed with large (short) periods during cold (warm) seasons.

In the Río de la Plata, differences in seasonal variability between the outer and the inner zone are observed. While Fig. 16 shows that the seasonal average spectra in O2 maintains its shape when changes from the more energetic condition of cold seasons to the less energetic one of warm seasons, Fig. 17 shows a change in the shape of the average spectra in I2 between seasons. In contrast to what was observed in the Atlantic and the outer RDP, in the intermediate and inner RDP, the wave energy of the SE quadrant (E to S) presents a minimum in autumn (AMJ), not accompanying the corresponding increase in energy of the SW quadrant (Fig. 17f).

### 3.3 Wave systems

First, Figs. 18 and 19 present results regarding the frequency of occurrence of different wave partitions and LTWS. Figure 18 presents the spatial distribution of the mode and the average of the number of partitions that make up a sea state at each node (i.e., the total number of wave spectral

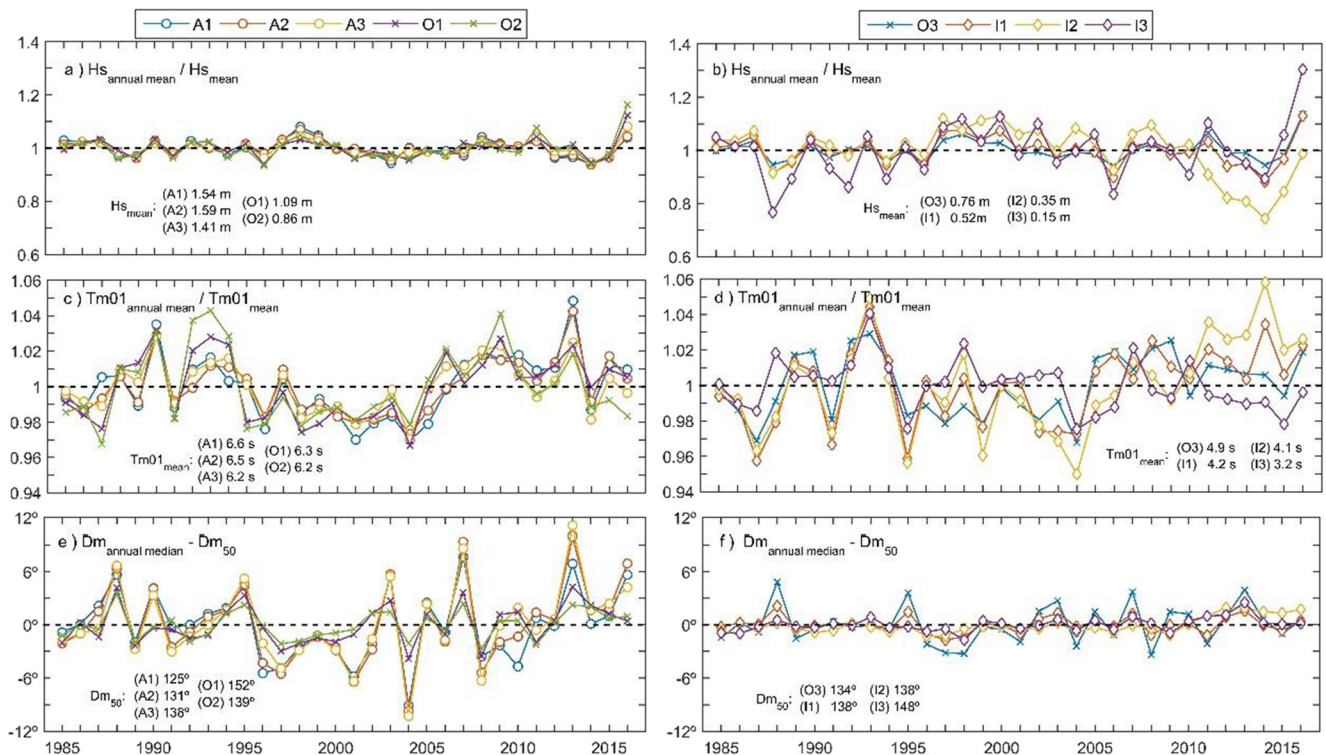
**Fig. 7** Spatial distribution of the coefficient of variation at annual scale for **a**  $H_s$ , **b**  $T_{m01}$ , and **c**  $D_m$ .



partitions over the number of sea states at each node). As described in Section 2.3, four LTWS were considered for grouping the wave partitions: wind seas, southern swells, eastern swells, and RDP swells. The relative frequency of these systems along the coast is presented in Fig. 19; this frequency

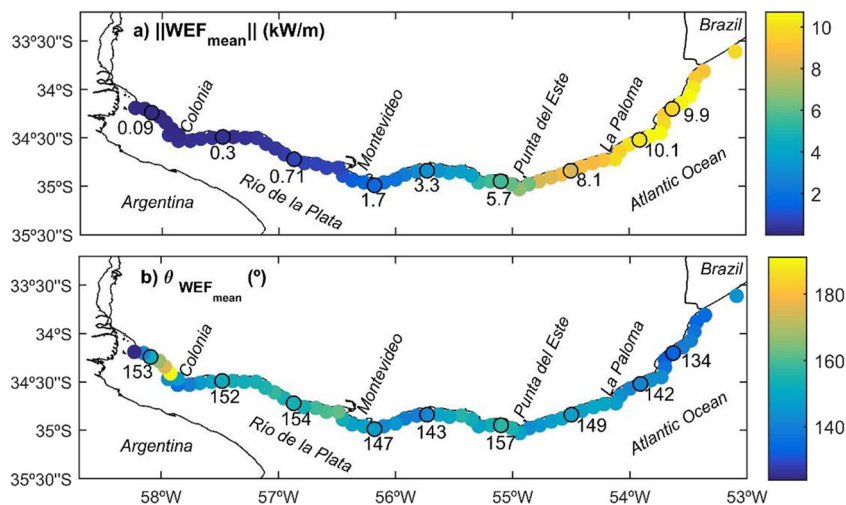
was calculated as the ratio between the amount of individual partitions classified as one LTWS and the total amount of partitions counted.

Figure 18b shows that the co-existence of two systems is the most frequent situation in the Atlantic. Moreover, Fig. 18a



**Fig. 8** Annual statistics of **a** and **b**  $H_s$ , **c** and **d**  $T_{m01}$ , and **e** and **f**  $D_m$  at points A1, A2, A3, O1, and O2 (left panels) and O3, I1, I2, and I3 (right panels)

**Fig. 9** Spatial distribution of mean wave energy flux: **a** magnitude and **b** direction



shows that in the Atlantic, the co-existence of more than two systems is more frequent than unimodal sea states, since the averages of the number of partitions are higher than two. In the outer RDP, although unimodal sea states are the most frequent, the averages of the number of partitions higher than one indicates that multimodal sea states are still a common situation. On the other hand, in the intermediate and inner RDP unimodal sea states are also the most frequent situation but an average lower than one indicates that multimodal sea states are infrequent. The zero values of modes in the innermost part of the RDP (Fig. 18b) shows that calm conditions are the most frequent situation west of Colonia.

It can be deduced from Fig. 19 that in the Atlantic and the outer RDP, most of the partitions are identified as swell, while in the Intermediate and Inner RDP, most of the partitions are wind seas. In the nodes where different swell systems can be distinguished, it was obtained that most of the partitions are identified as southern swells (43–49%, Fig. 19d), then they are identified as eastern swells (28–40%, Fig. 19b), and finally as wind seas (17–25 %, Fig. 19b).

Then, Figs. 20, 21, 22, 23, 24, 25, and 26 present results summarizing the average behavior of each LTWS at each node. Figures 20, 21, and 22 show mean of  $H_s$  and  $T_p$  and the median of  $D_p$  for each LTWS, respectively, while Figs. 23

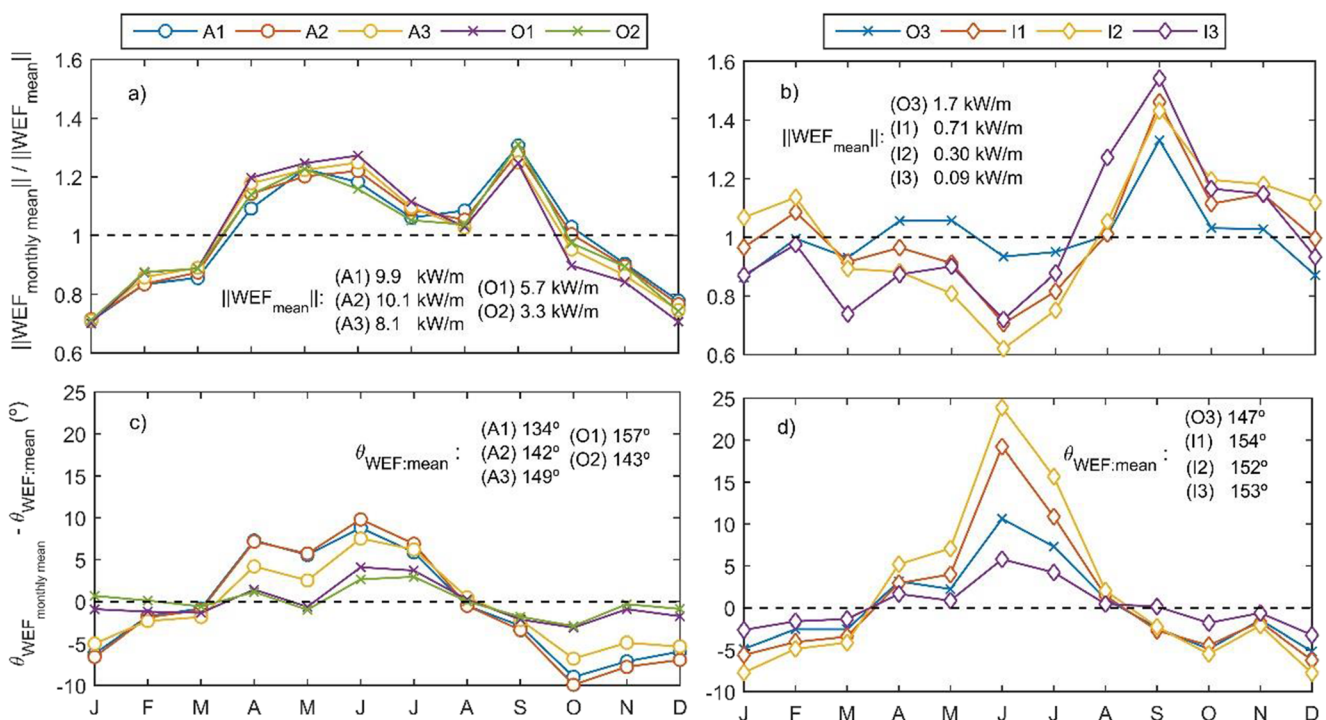
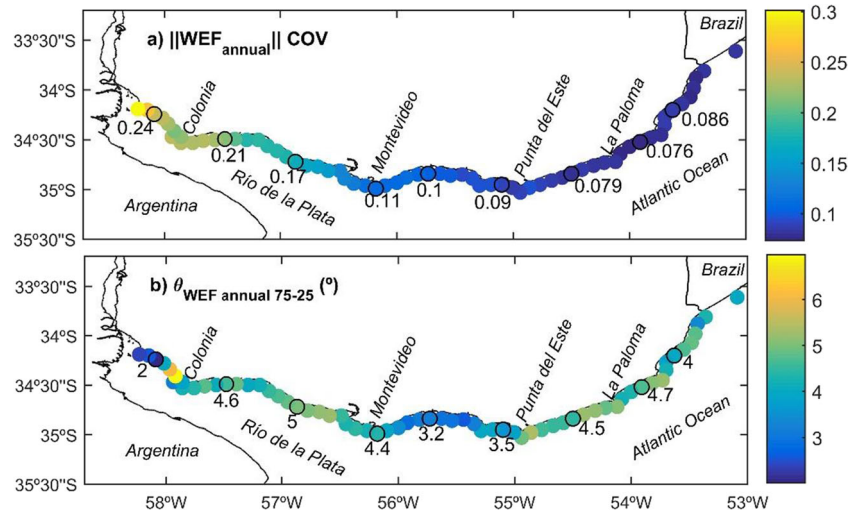


**Fig. 10** Annual cycle of mean wave energy flux at **a** and **c** nodes A1, A2, A3, O1, and O2 (left panels) and **b** and **d** nodes O3, I1, I2, and I3 (right panels)



**Fig. 11** Spatial distribution of the coefficient of variation at annual scale of the mean wave energy flux: **a** magnitude and **b** direction



to 24 show the average spectra of the three LTWS for nodes A2 and O2 (the figure for I2 is included in the supplementary material). Figure 25 presents the spatial distribution of the relative contribution of each LTWS to the total WEF; complementarily, Fig. 26 shows the vector decomposition of the WEF at the nine selected nodes.

From Figs. 25 and 26, it follows that more than a half of the wave energy that reaches the Atlantic coast comes from southern swells. The average properties of this LTWS practically do not vary along the Atlantic coast, showing mean  $H_s$ , mean  $T_p$ , and median  $D_p$  around 0.85 m, 10.5 s, and  $165^\circ$ , respectively (Figs. 20d, 21d, and 22d). As expected for swells, it presents a narrow-banded average spectrum with a peak around  $165^\circ$  and 11.7 s (Fig. 23). On the other hand, eastern swells are less energetic and shorter than southern swells (see Figs. 25b and 21b, respectively), and a change in their mean properties occurs around La Paloma, where its mean  $H_s$  declines from 0.75 to 0.65 m (Fig. 20b). A similar decline around La Paloma is observed for wind seas mean  $H_s$  (Fig. 20a) which is

accompanied by a clockwise rotation, by which wind seas  $D_p$  median goes from  $97$  to  $114^\circ$  (Fig. 22a). Then, west to Punta del Este, the wind seas rotate again to the south, and then throughout the RDP, its  $D_{p50}$  remains between  $163$  and  $180^\circ$  (Fig. 22a). In the outer RDP,  $H_s$  ( $T_{m01}$ ) mean of wind seas decays from 1 m (6 s) near Punta del Este to 0.85 m (5 s) near Montevideo (Figs. 20a and 21a). In this region, the two swell systems converge into one (i.e., RDP swells) and dissipate. This is clearly seen in Fig. 26d,e, and f. Regarding the intermediate and inner RDP, its wave climate is completely dominated by wind seas (Fig. 25a), whose  $H_s$  ( $T_{m01}$ ) mean decays from 0.85 m (5 s) near Montevideo to 0.6 m (3.6 s) at the innermost node (Figs. 20a and 21a). Considering that in the RDP the energy of the SW quadrant is not negligible (Fig. 24), the decay of  $H_s$  and  $T_{m01}$  are explained not only by a decrease in water depth but also by fetch limitations.

Results related with the intra-annual and inter-annual variability of the LTWS are presented in Figs. 27, 28, 29, and 30. Figures 27, 28, and 29 show mean annual cycle for each

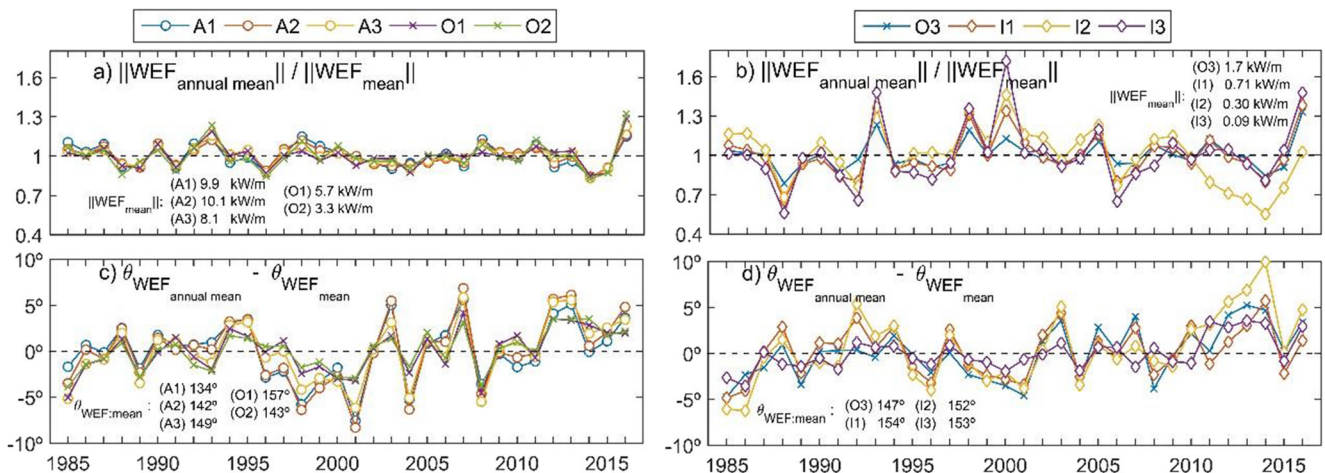


**Fig. 12** Annual mean of wave energy flux: **a**, **b** magnitude and **c**, **d** direction. Nodes A1, A2, A3, O1, and O2 (left panels, **a** and **c**) and nodes O3, I1, I2, and I3 (right panels, **b** and **d**)



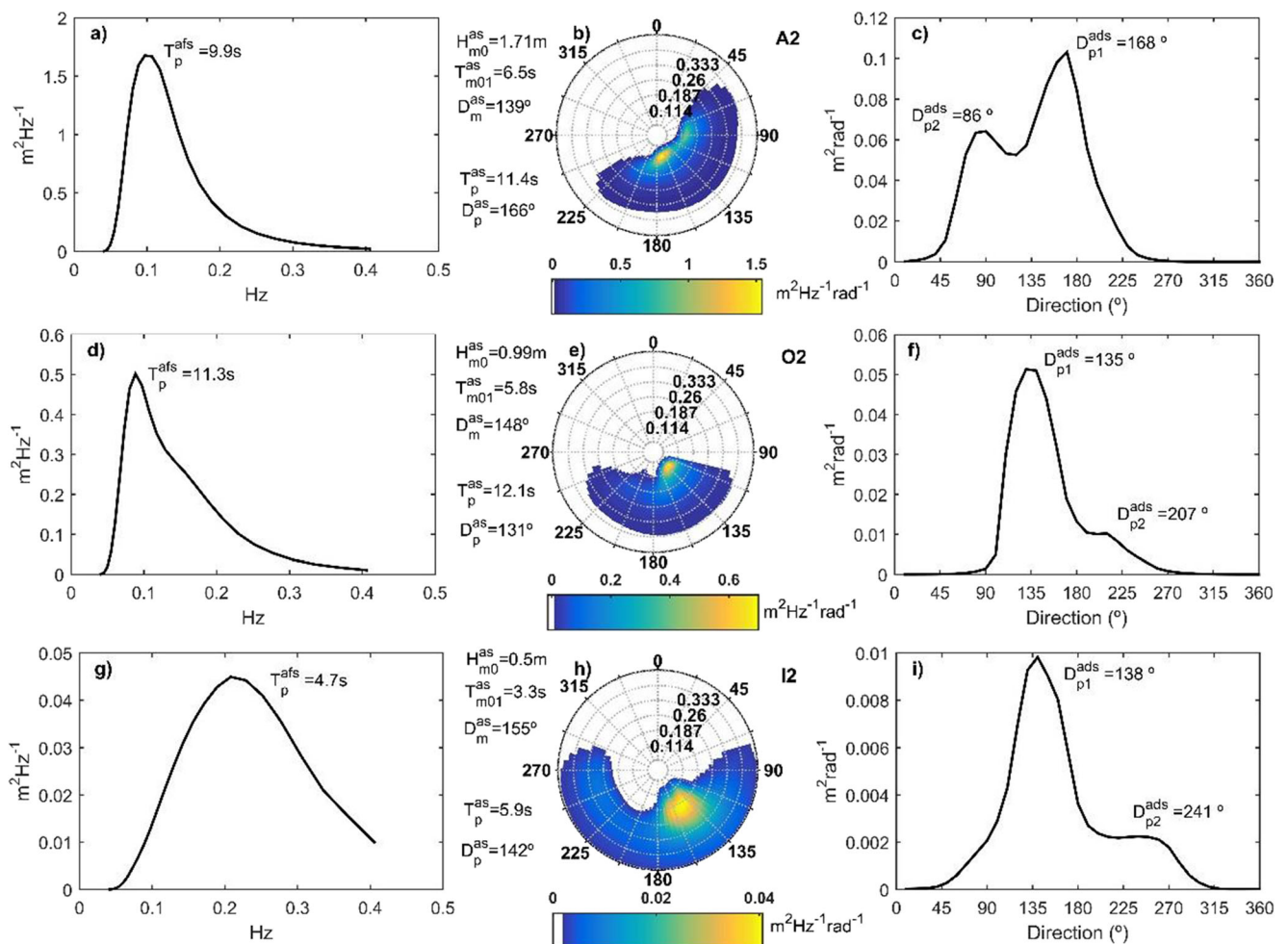


**Fig. 13** Average spectra at node A2 (a, b, c), node O2 (d, e, f), and node I2 (g, h, i). One-dimensional average spectrum along frequencies (left panels, a, d, and g), two-dimensional average spectra (central panels, b, e, and h), and one-dimensional average spectrum along directions (right panels, c, f, and i)

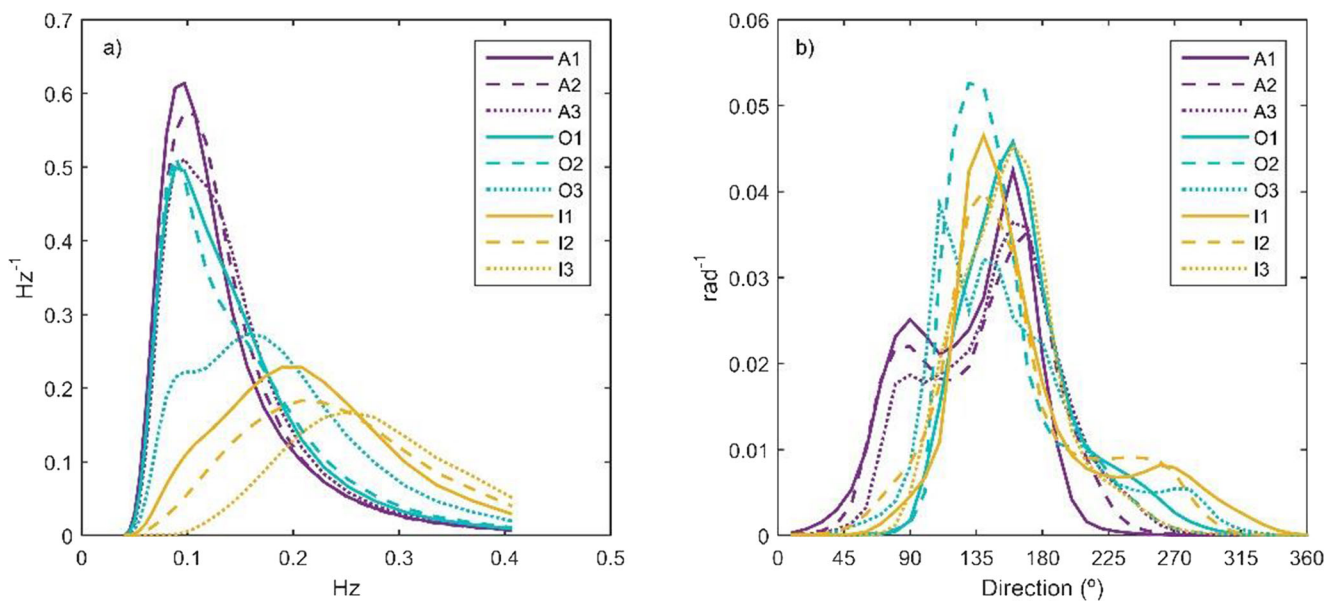


**Fig. 14** Normalized average spectra at the nine selected nodes: **a** along frequencies and **b** along directions

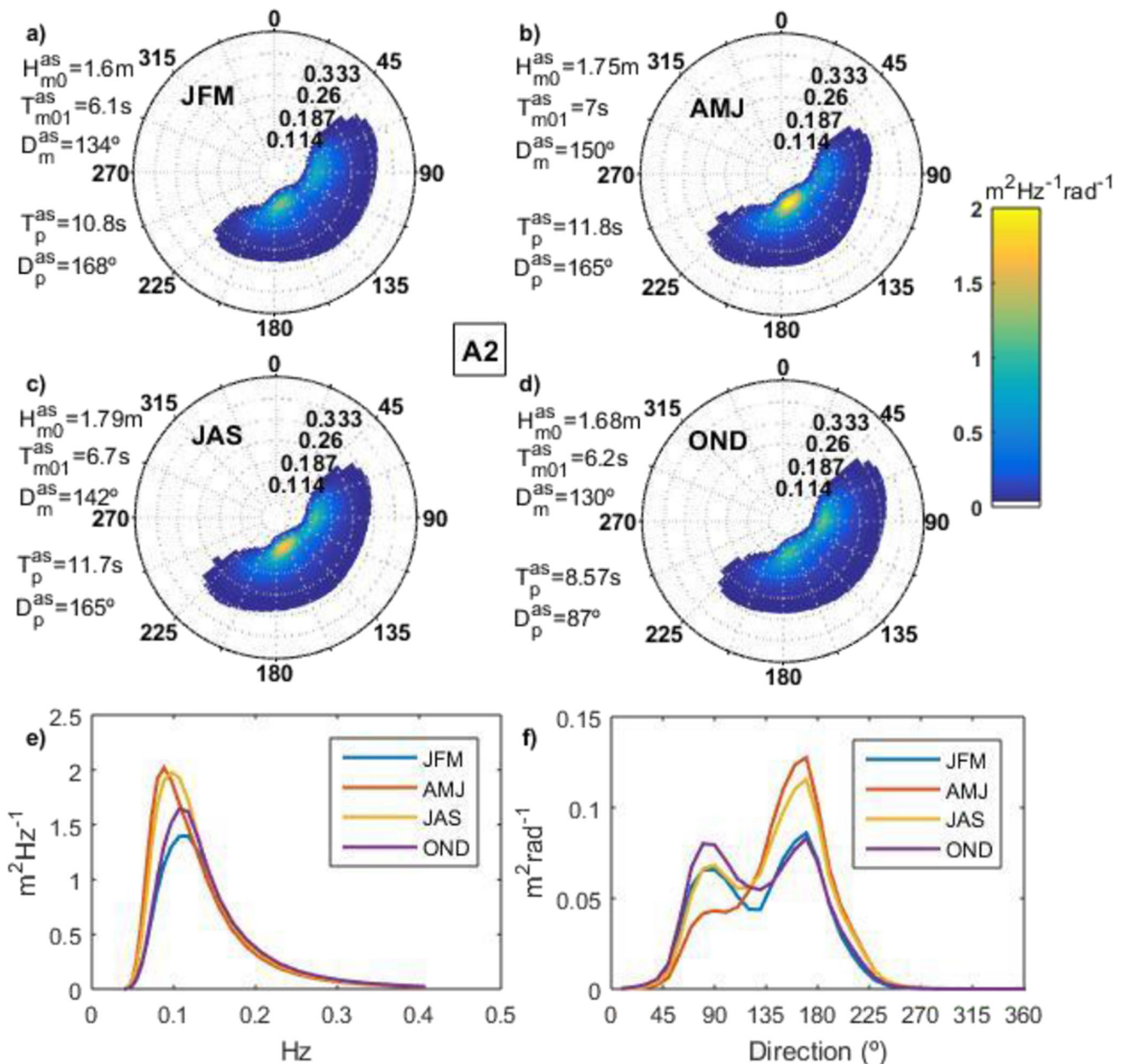


**Fig. 15** Seasonal average spectra at A2. Two-dimensional average spectrum for **a** summer, **b** autumn, **c** winter, and **d** spring. One-dimensional seasonal average spectra: **e**) along frequencies and **f**) along directions

analyzed variable (i.e., percentage of occurrence,  $H_s$ ,  $T_p$ ,  $D_p$ , and WEF magnitude and direction) and LTWS at nodes A2, O2, and I2, respectively, while Fig. 30 shows time series of mean annual values for  $T_p$  and WEF direction at the same locations (the figures for the other variables are provided in the supplementary material).

It is observed that southern swells increase their occurrence from April to September, a period during which average  $H_s$  and  $T_p$  are higher than the annual average (Fig. 27). This pattern of higher  $H_s$  and  $T_p$  during cold seasons is also observed for wind seas (Figs. 27, 28, and 29). A different pattern

is observed for eastern swells; this system presents higher  $H_s$  and  $T_p$  from September to November. However, it is noted that the three systems show a peak in the annual cycle of  $H_s$  in September (Fig. 27b). This coincidence explains the spike in September observed in the annual cycle of total  $H_s$  (Fig. 6a and b). In terms of directions, the swell systems of the Atlantic practically do not vary throughout the year (Fig. 27d and f), but the wind seas rotate in a wide arc, rotating southward in cold seasons (April to September) and eastward during warm seasons (October to March), which is observed in the three regions (Figs. 27, 28, and 29). Due to the orientation and

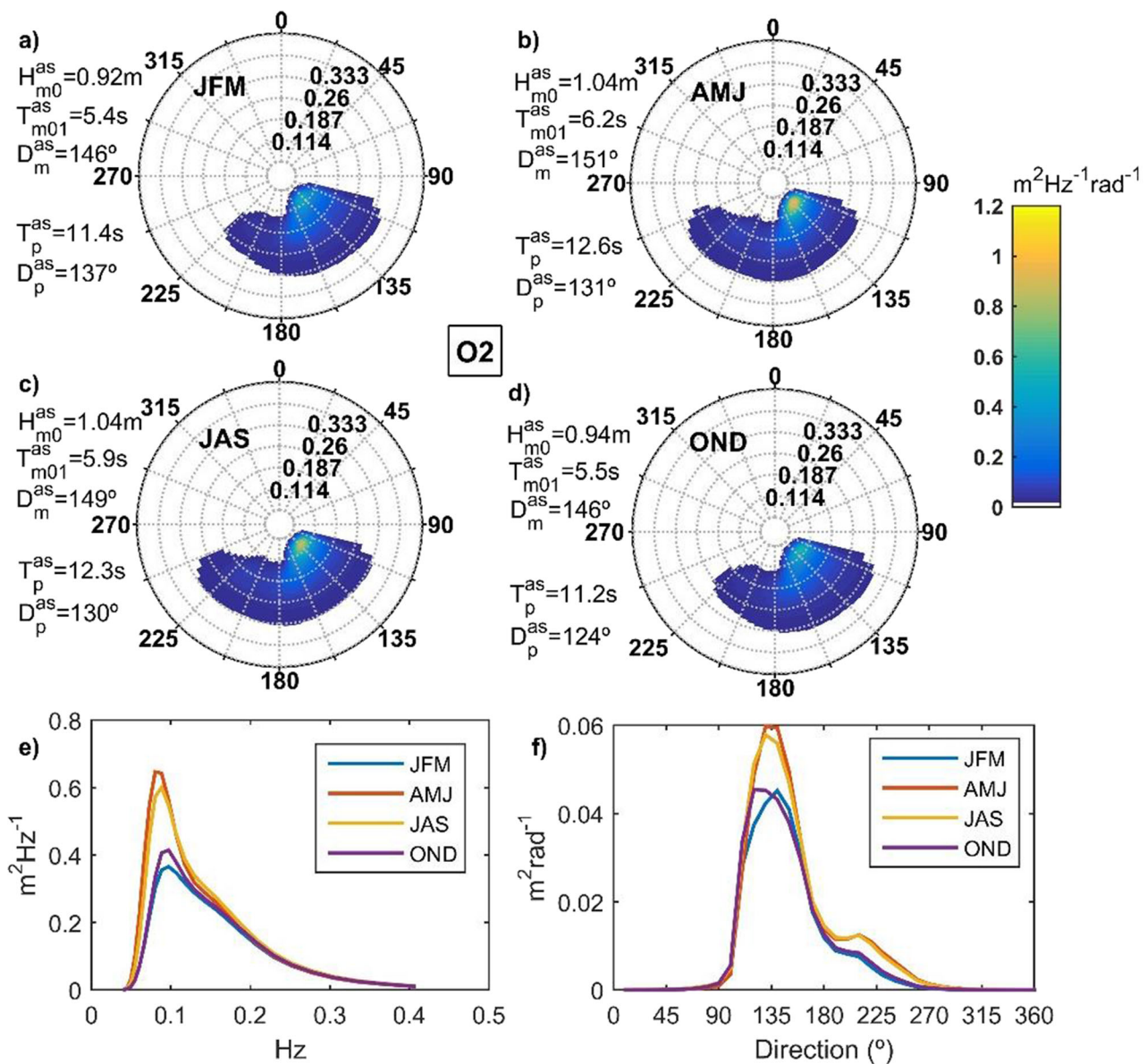


**Fig. 16** Seasonal average spectra at O2. Two-dimensional average spectrum for **a** summer, **b** autumn, **c** winter, and **d** spring. One-dimensional seasonal average spectra: **e**) along frequencies and **f**) along directions

geometry of the estuary, this rotation is accompanied by a fetch reduction and, therefore, by a decrease of  $H_s$  and  $T_{m01}$  of wind seas in winter in the RDP (Figs. 28c and d, and 29c and d). This winter decrease is observed for total  $H_s$  (Fig. 6b) but not for total  $T_{m01}$  (Fig. 6d); what is the difference in both annual patterns and its explanation lies in the different impact that RDP swells have on the means of total  $T_{m01}$  and  $H_s$ , RDP swells are composed of southern and eastern swells, so the directional variations throughout the year (Fig. 28d and f) is consistent with the higher influence of southern swells (eastern swells) in winter (spring).

Regarding inter-annual variability, the decomposition into systems reveals which system is behind the main long-term trends and cycles observed when total parameters are analyzed.

On one hand, the long-term clockwise rotation of the wave climate is associated with wind seas (Fig. 30b, d, and e). On the other hand, the cycle of almost 20 years observed in periods in the Atlantic is associated to southern swells (Fig. 30a)

Lastly, the results of the different correlation analysis are presented in Fig. 31 and Table 2. The delimitation of the generation zones of the swell systems can be seen in Fig. 31a and b that shows the maps of maximum correlation between  $H_s$  and the wind velocity projection in the great circles. The matrices of spatial correlation for the different systems at different nodes are shown in Fig. 31c, d, and e. The matrix corresponding to wind seas (Fig. 31c) shows that there are four regions where wind seas are strongly correlated: in the intermediate and inner RDP (west to Montevideo, nodes 37 to



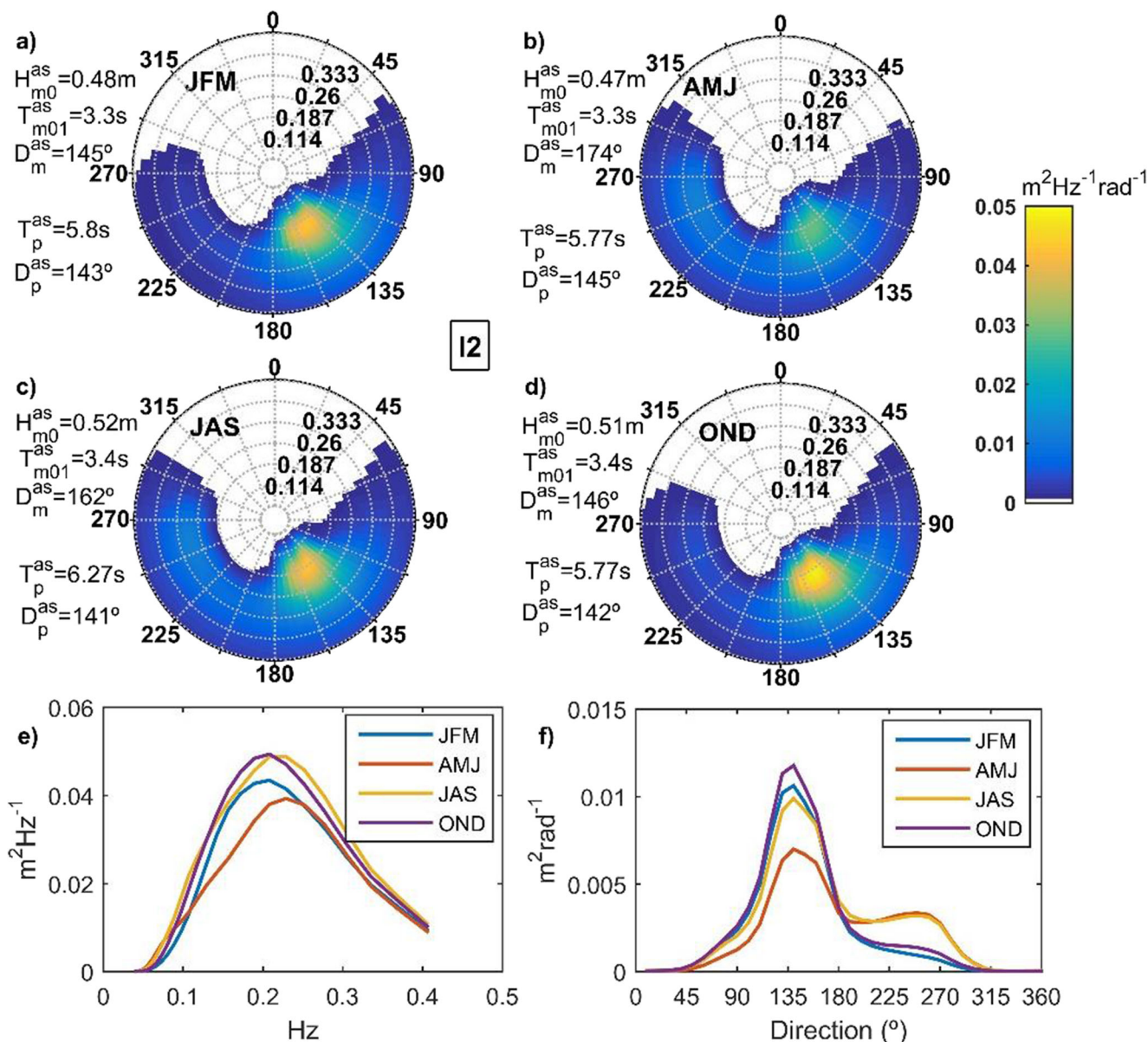


**Fig. 17** Seasonal average spectra at I2. Two-dimensional average spectrum for **a** summer, **b** autumn, **c** winter, and **d** spring. One-dimensional seasonal average spectra: **e** along frequencies and **f** along directions

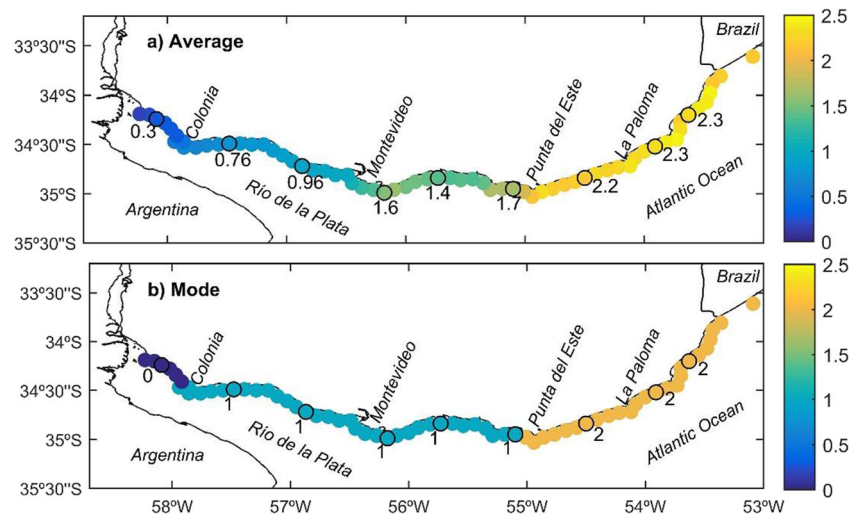
65), in outer RDP (Montevideo – Punta del Este), in the Atlantic from Punta del Este to La Paloma, and lastly, from La Paloma to the east. Regarding swells, it is observed that RDP swells present larger correlation with southern swells (Fig. 31d) than that with the eastern swells (Fig. 31e). Finally, Table 2 shows that significant correlations with AAO were found but not with SOI. The correlations with AAO are positive for wind seas and eastern swells and negative for southern swells. These opposite signs seem to explain why a significant correlation is not observed between the RDP swells and AAO and also when total  $H_s$  is considered, exposing one of the benefits of considering different systems for the analysis, as they unmask this type of linkages between waves and climate patterns.

#### 4 Discussion

Obtained results are in agreement with and reinforce what was suggested by previous works in terms of the distinction made between the wave climate at the Atlantic coast, the outer RDP coast, and the intermediate and inner RDP coast (Santoro et al. 2017; Solari et al. 2018). On the one hand, in the Atlantic coast around 80% of the wave partitions are classified as swells (Fig. 19), accounting for almost 75% of the incident WEF (Fig. 25); moreover, as it was pointed out by Romeu et al. (2015), multimodality of the spectrum is a distinctive feature of this zone: a sea state is composed on average of 2.3 wave partitions (Fig. 18). On the other



**Fig. 18** Spatial distribution of the number of wave systems that make up a sea state: **a** average and **b** mode



hand, aligned with Dragani and Romero (2004), to the west of Montevideo (the intermediate and inner RDP), most of the sea states are unimodal (Fig. 18) and the wave climate is dominated by wind seas, both in terms of frequency of occurrence (Fig. 19) and incident WEF (Fig. 25). The zone in between these two (the outer RDP) is characterized by a smooth transition between the two wave climates, with the number of wave partition decreasing from over two to one (Fig. 18), and with swells converging in the direction of the estuary’s axis (approx. 125°; Fig. 22) and dissipating due to decreasing depths (Fig. 25). The WEF contributed by the swell (wind sea) systems decreases (increases) gradually from Punta del Este toward the west.

Regarding the Atlantic coast, a distinctive feature of its wave climate is bimodality. Average spectra show two peaks, one associated with south directions and the other with east directions (Figs. 13, 14, and 15); both swells and wind seas present this bimodality (Fig. 23). Swells were grouped in accordance to these two modes and analyzed separately. Southern swells are the most frequent, accounting for almost half of the wave partitions (Fig. 19), occurring throughout the Atlantic coast with mean  $H_s$  of 0.85 m, mean  $T_p$  of 10.5s and median  $D_p$  around 165° (Figs. 20, 21, and 22); eastern swells on the other hand are less frequent (approx. 35 % of the wave partitions; Fig. 19) and less energetic, with mean  $H_s$  around 0.75 m (0.65 m) to the east (west) of La Paloma, mean  $T_p$  around 8.2 s, and median  $D_p$

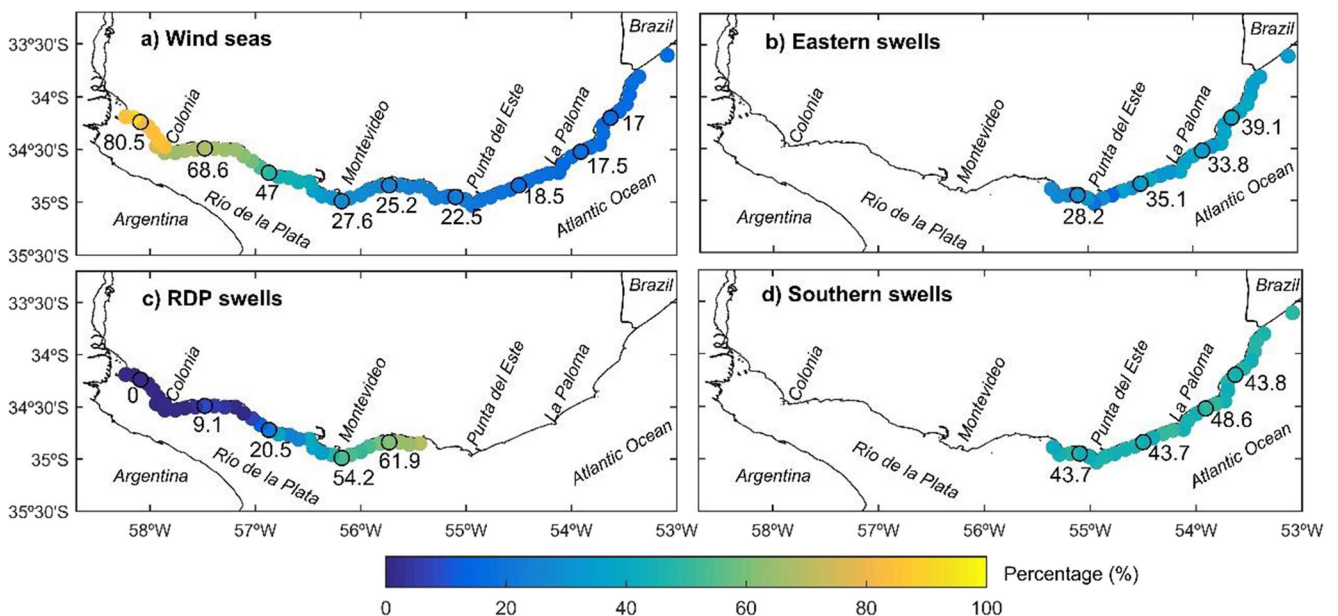


**Fig. 19** Spatial distribution of the frequency of occurrence of **a** wind seas, **b** eastern swells, **c** RDP swells and **d** southern swells.

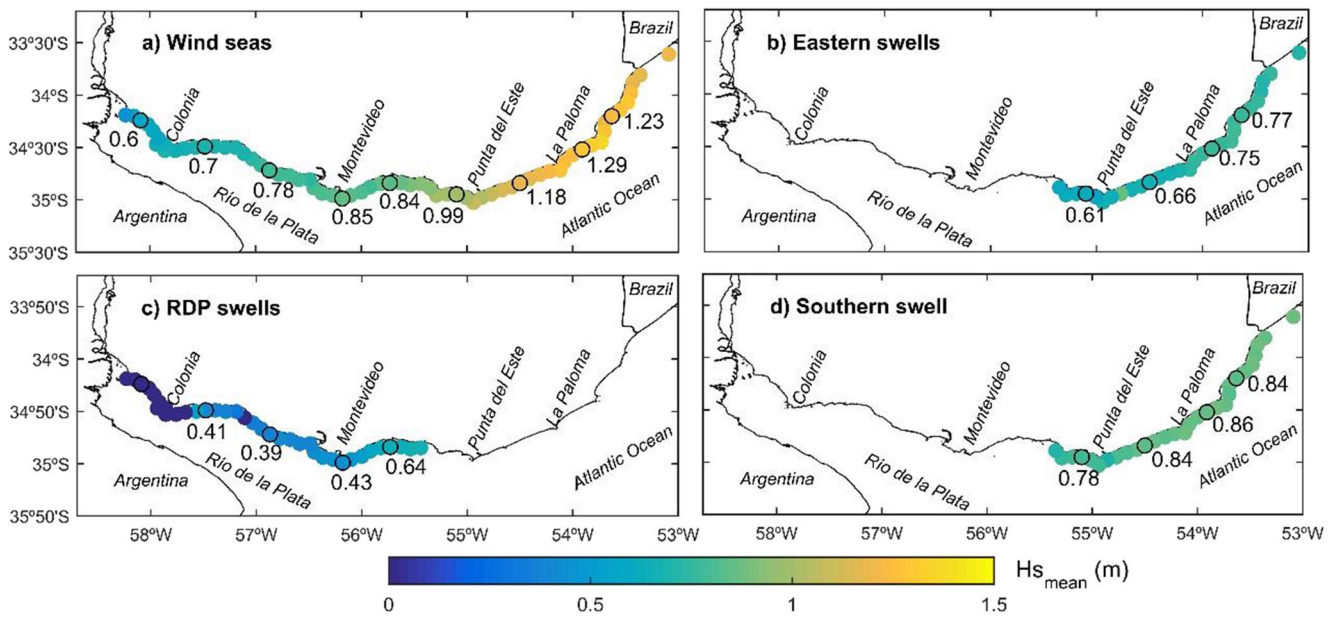


**Fig. 20** Spatial distribution of the mean of  $H_s$  corresponding to **a** wind seas, **b** eastern swells, **c** RDP swells, and **d** southern swells

around  $85^\circ$  (Figs. 20, 21, and 22). This is the area with the highest wind seas, and as was the case with eastern swells, they show different behavior on both sides of La Paloma: to the east, mean  $H_s$  is approx. 1.25 m, while to the west, it decreases down to 1 m in Punta del Este (Fig. 20). This change in La Paloma is also observed when looking at wind sea directions, which have a median  $D_p$  of around  $95^\circ$  ( $115^\circ$ ) to the east (west) of La Paloma (Fig. 22), and is confirmed by the analysis of the spatial correlation of the wind seas (Fig. 31c). This change in the wave climate at La Paloma is attributed to the change in the orientation of the

coast; to the west of La Paloma, the coast is more southward oriented, while to the east, it is more eastward oriented, being more exposed to eastern swells and wind seas coming from the east. When looking at the integral wave parameters, this translates into higher waves and a counterclockwise rotation of the waves eastward of La Paloma, in agreement with Alonso et al. (2015): in east (west) of La Paloma, mean  $H_s$  is around 1.55 m (1.4 m), median  $D_p$  around  $128^\circ$  ( $138^\circ$ ), WEF magnitude around 10 kW/m (8 kW/m), and WEF direction around  $140^\circ$  ( $150^\circ$ ) (Figs. 3, 5, and 9, respectively).

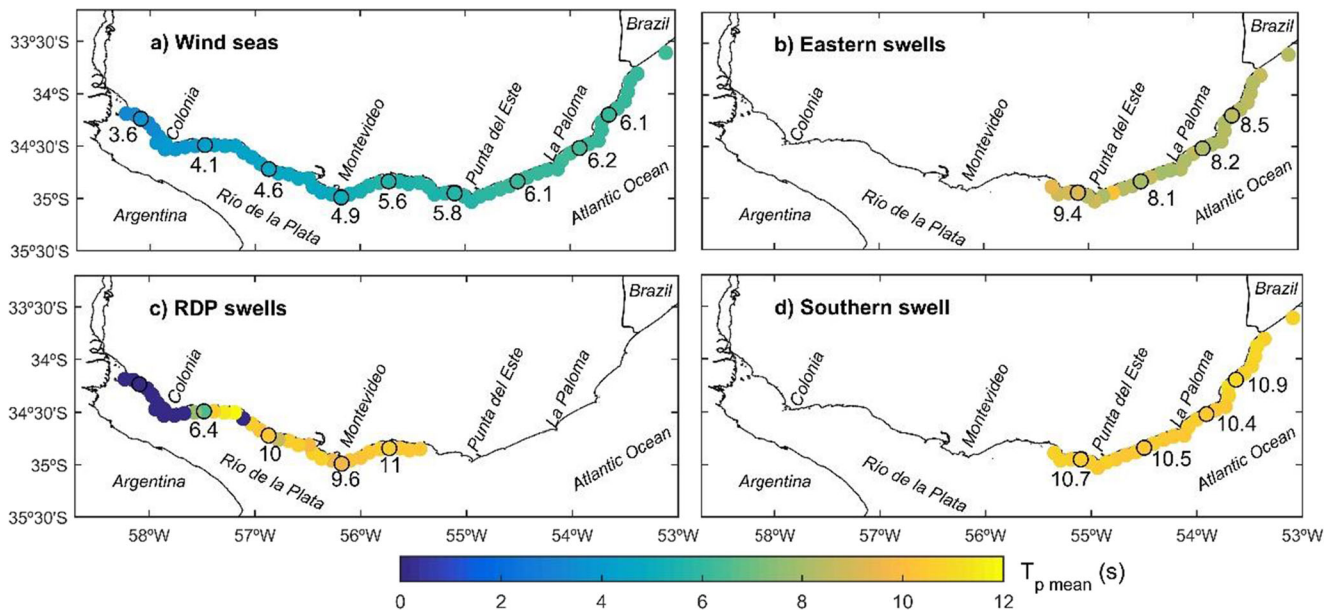


**Fig. 21** Spatial distribution of the mean of  $T_p$  corresponding to **a** wind seas, **b** eastern swells, **c** RDP swells, and **d** southern swells

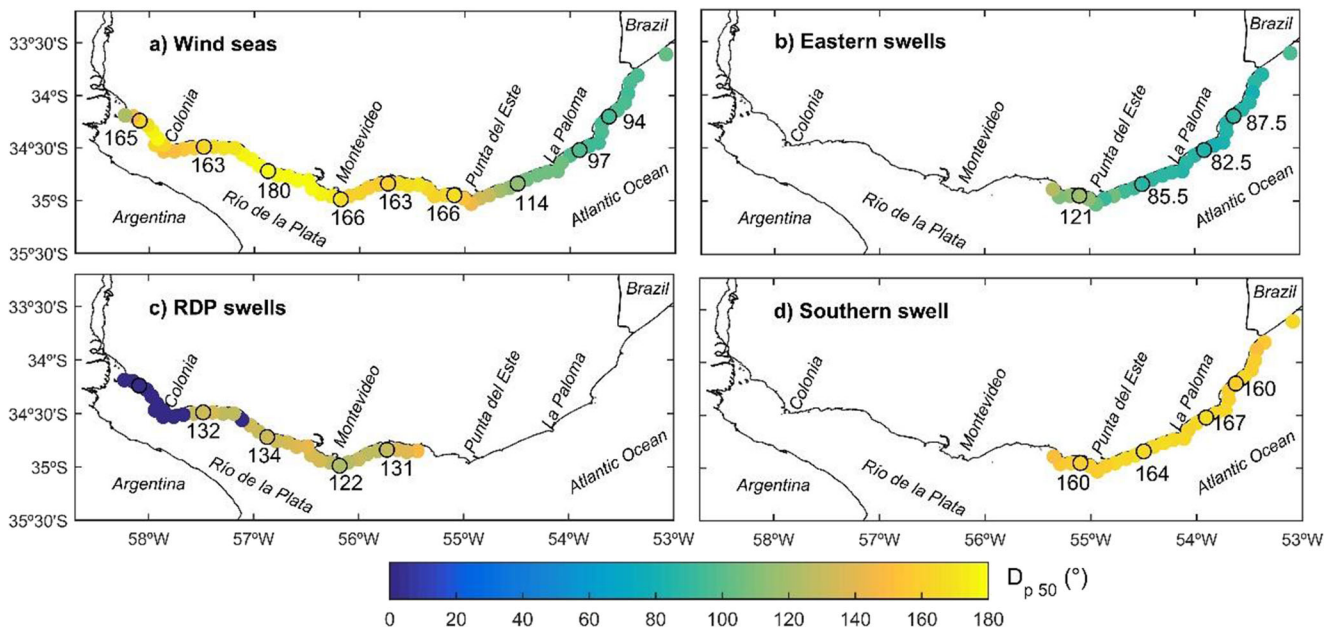


**Fig. 22** Spatial distribution of the median of  $D_p$  corresponding to **a** wind seas, **b** eastern swells, **c** RDP swells, and **d** southern swells

The outer RDP is characterized by the decay of the wave energy along its coast. This is explained mainly by swell dissipation and, to a lesser extent, by the decreasing depth affecting the development of wind seas, as it

appears from analyzing the decomposition diagrams of the WEF at points O1 to O3 (Fig. 26), while the energy of swells at O3 is almost seven times lower than the sum of WEF

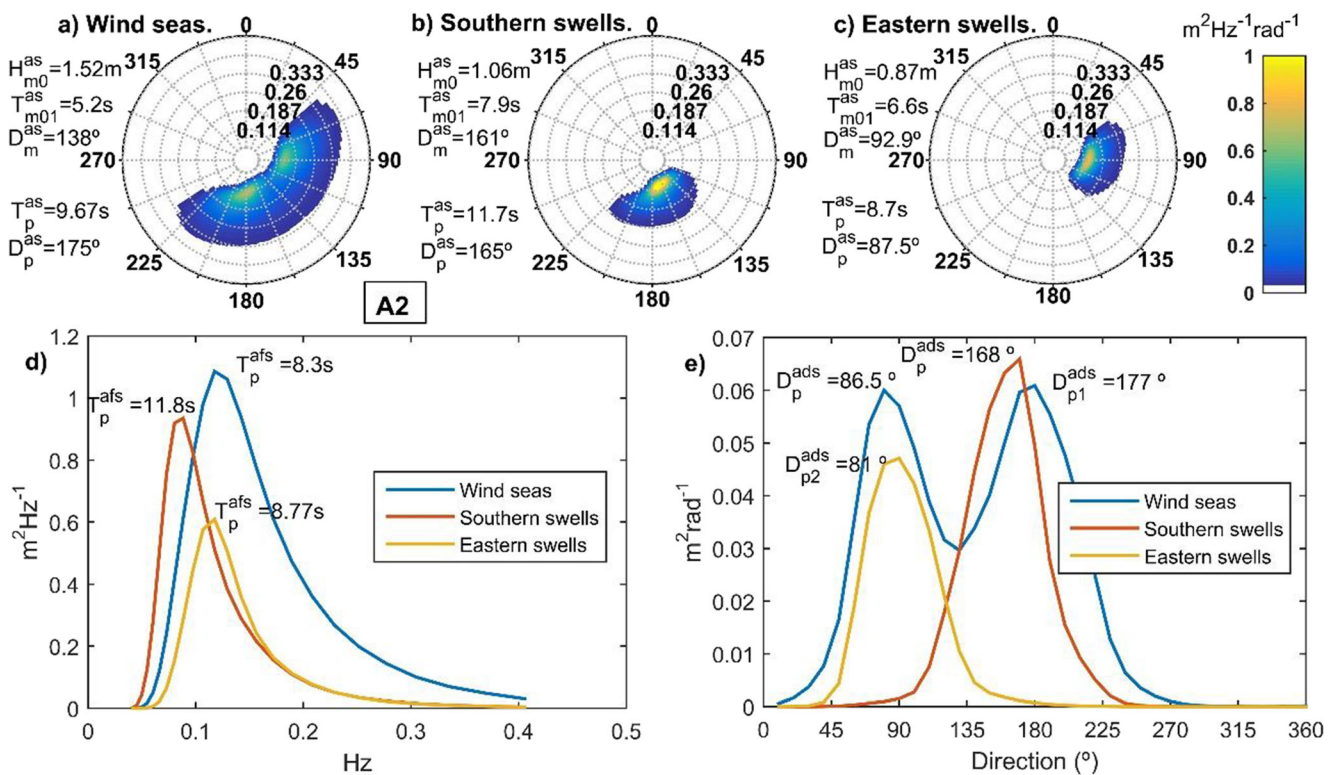


**Fig. 23** Average wave system spectra at A2. Two-dimensional spectrum of **a** wind seas, **b** southern swells, and **c** eastern swells. One-dimensional spectra: **d** along frequencies of all systems and **e** along directions of all systems



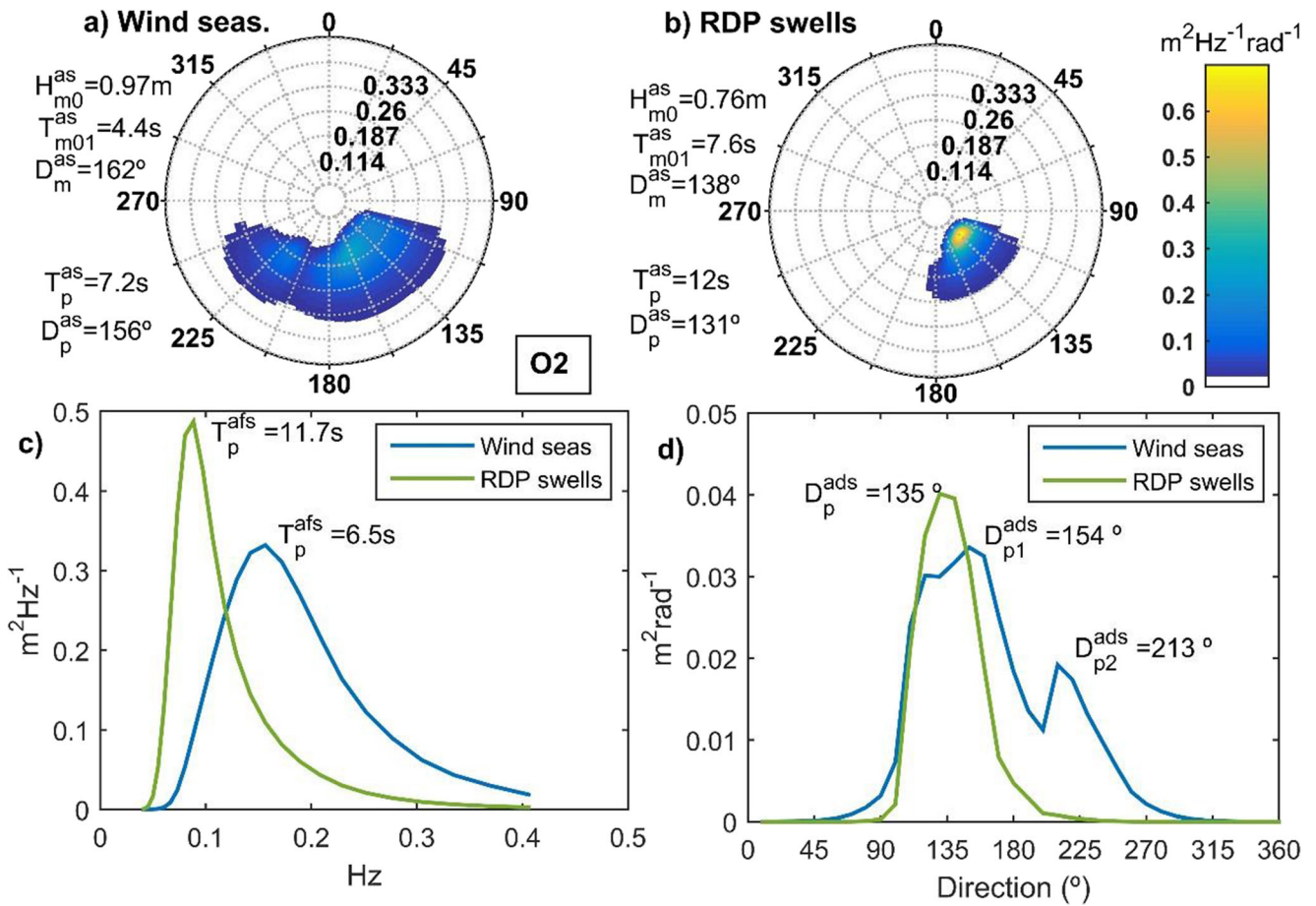


**Fig. 24** Average wave system spectra at O2. Two-dimensional spectrum of **a** wind seas, **b** southern swells, and **c** eastern swells. One-dimensional spectra: **d** along frequencies of all systems and **e** along directions of all systems

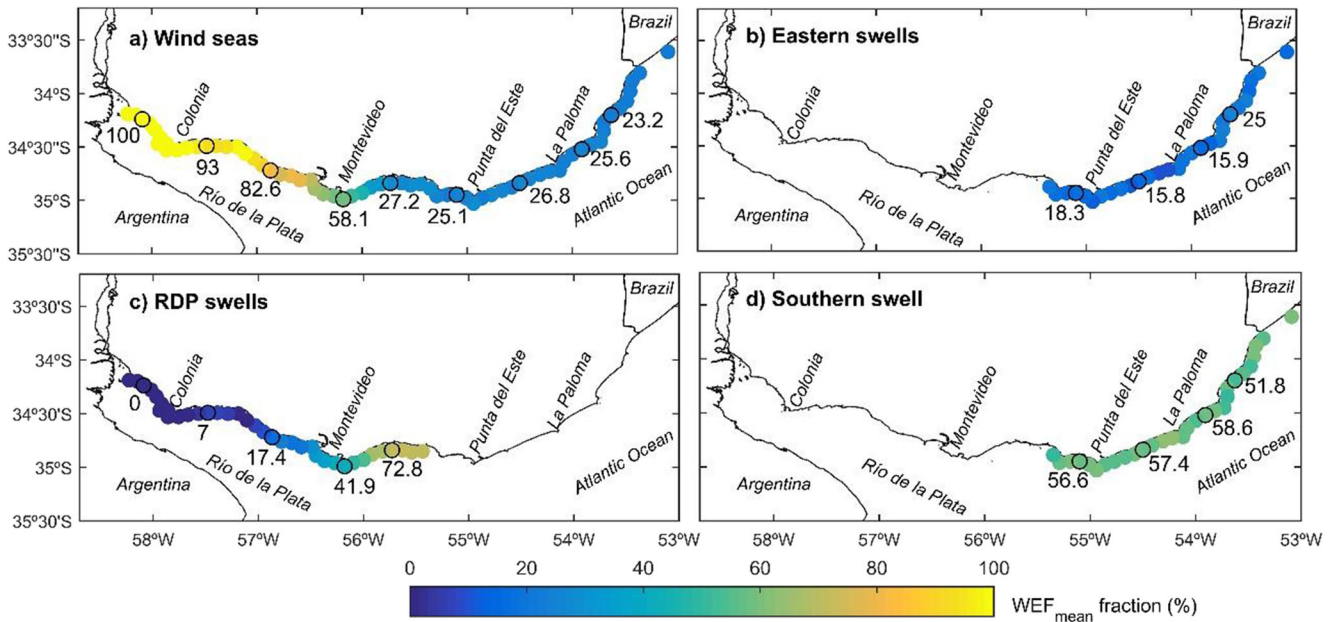


**Fig. 25** Spatial distribution of the fraction of the mean wave energy flux corresponding to **a** wind seas, **b** eastern swells, **c** RDP swells, and **d** southern swells



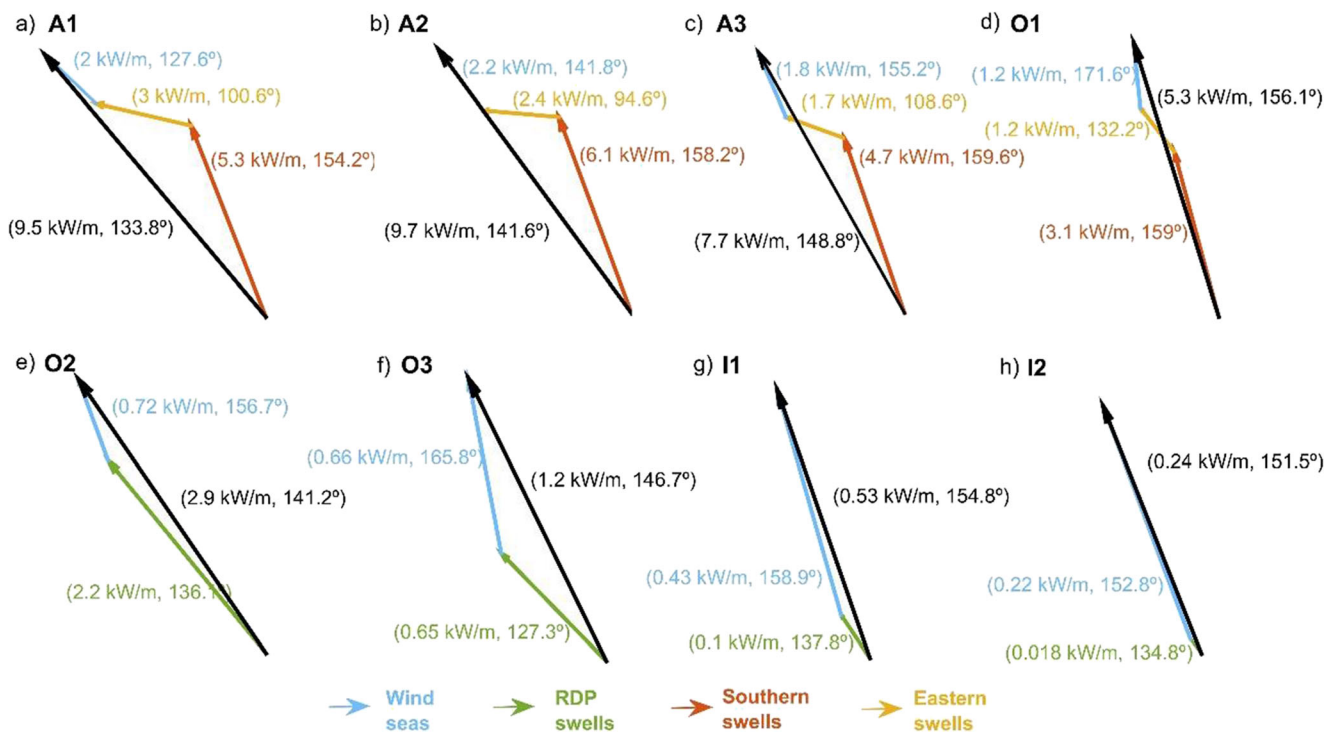


Fig. 26 Decomposition of mean wave energy flux by systems

magnitude of southern and eastern swells at O1. The different contribution of the two processes is also evidenced by how the parameters of the LTWS evolve between Punta del Este and Montevideo (Fig. 20), and while wind seas mean  $H_s$  decreases from 1 m to 0.85 m, swells mean  $H_s$  reduction is larger, from about 0.72 (adding southern and eastern swells) to 0.4 m. Taken together, the decline in both swells and wind seas results in that mean  $H_s$  (i.e., integral parameter) decreases from around 1.2 to 0.75 m (Fig. 3), and mean WEF decreases from 6 to 1.7 kW/m (Fig. 9). Moreover, as swells' decay is larger than that of wind seas, the periods are also affected, with mean  $T_{m01}$  decreasing by almost 1.5 s (Fig. 4), and  $T_p^{afs}$  decreasing from 10.5 to 6 s (Figs. 13 and 14). Beyond energy decay, wave climate in this area is also significantly affected by refraction: as evidenced by the swells directional average spectrum, swells tend to align with the axis of the estuary (135°; Fig. 24), completely losing any trace of bimodality (compare Fig. 23e with Fig. 24d). In comparison, wind seas show little variation in terms of median  $D_p$  (Fig. 22a) between Punta del Este and Montevideo, so the rotation observed in the median  $D_p$  (integral parameter; Fig. 5) is mainly attributed to swell refraction. Regarding wind seas, a distinctive feature in this area is its strong spatial correlation (Fig. 31c) and the increase of the relative importance of the waves from the SW quadrant (S to W) (Figs. 13, 14, and 24), product of the change in the alignment of the coast.

The wave climate in the intermediate and inner RDP is governed by wind seas that show a strong spatial correlation in the area (Fig. 31c), and whose energy gradually decreases to the west of Montevideo (Figs. 20 and 26). There are two factors explaining this pattern. On the one hand, there are water depths decreasing towards the inner part of the estuary: as wave generation in the area is depth-limited, a decrease in depth results in lower and shorter waves. On the other hand, as the estuary has a NW–SE orientation and a funnel shape, fetches corresponding to the SW quadrant also decrease towards the inner RDP.

With regard to severe conditions, it is noted that the difference between Atlantic and RDP coasts is lower for the  $H_s$  99th percentile than for mean  $H_s$  (Fig. 3), probably because extreme conditions are wind seas, sharing the same forcing at both environments, with differences coming from depths and fetches. It is noted that no extremer conditions than the 99th percentile were analyzed as it might require a deeper look into possible underestimations coming from CFSR winds (see e.g., Campos et al. 2018; Campos et al. 2019).

Regarding variability (as measure by COV), it is noted that for  $H_s$  and  $T_{m01}$ , it is larger in the RDP than in the Atlantic, increasing towards the inner RDP (Figs. 3 and 4). This is in agreement with the increase in the relative importance of wind seas in the RDP, since the short-term variability of local winds is translated directly to the wave

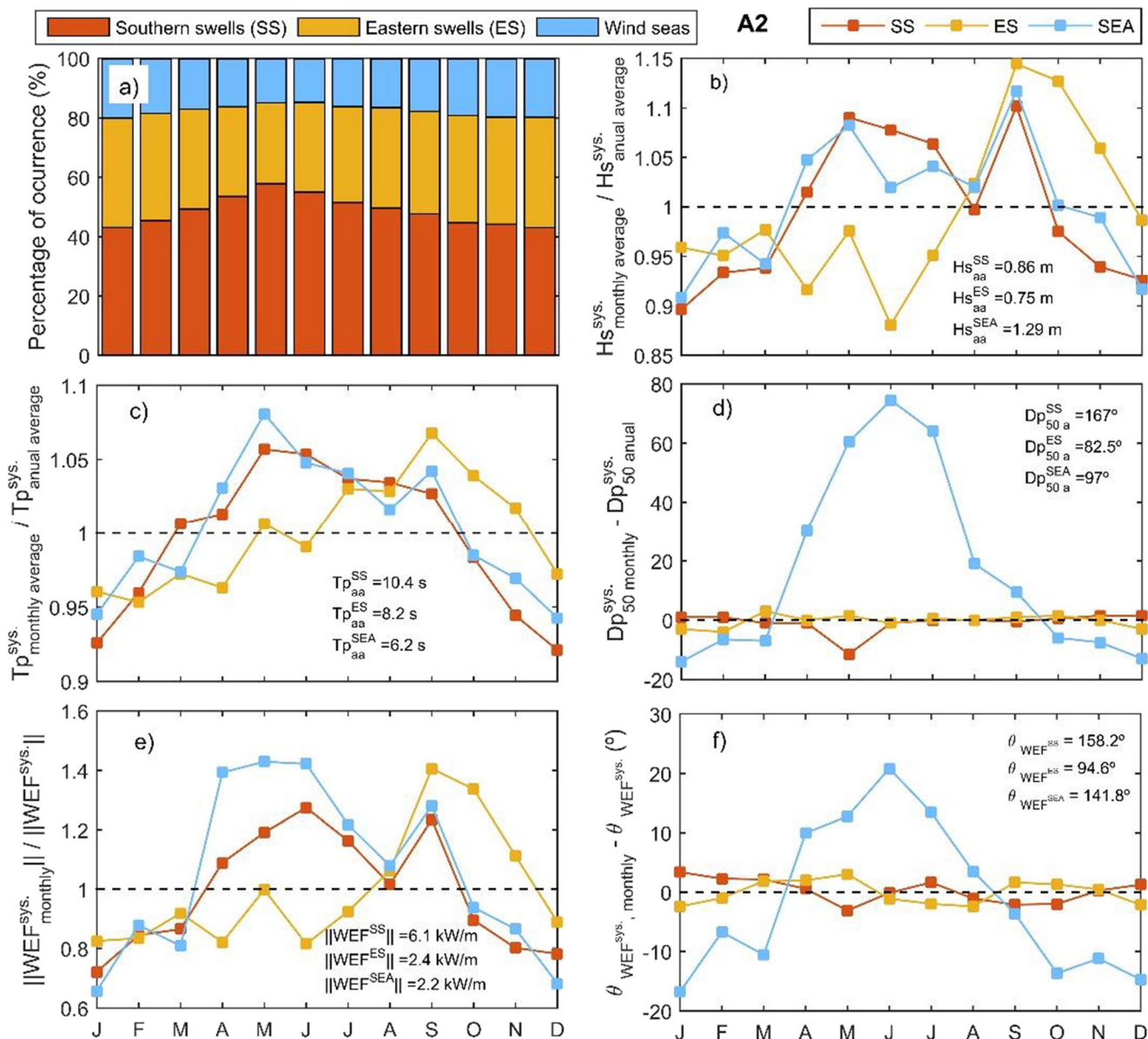


**Fig. 27** Annual cycles of different wave systems parameters at A2. **a** Frequency of occurrence, **b**  $H_s$ , **c**  $T_p$ , **d**  $Dp_{50}$ , **e** magnitude of the mean wave energy flux, and **f** direction of the mean wave energy flux

climate; in the areas where swells are more relevant, the variability is reduced. On the other hand, due to bimodality of the wave climate in the Atlantic, wave directions present a larger variability there than in the RDP (Fig. 5). From Fig. 6, it follows that variability in wave directions is mostly related with its annual cycle; when looking at the LTWS, it is clear that the annual cycle of the wave direction has a twofold explanation (Figs. 27, 28, and 29): on the one hand, there is a pronounced annual cycle in wind seas directions all along the coast; on the other hand, at the Atlantic coast, there is a change in the relative frequency of the two swell systems along the year, with the southern (eastern) swells being more frequent during

cold (warm) seasons (Fig. 27). In addition, southern swells are longer and more energetic during cold seasons in the Atlantic (Fig. 27b and c), a pattern that is also observed in swells in the outer RDP (Figs. 28 and 29), and is consistent with the highest cyclogenesis frequency observed for cold seasons by previous studies of regional winds (De Oliveira et al. 2011). So, between April and September, southern swells and swells in the RDP are more frequent and show larger periods than their annual average, which in turn translates into the annual cycle of mean periods shown in Fig. 6c and d. Unlike the southern swells, the annual cycle of eastern swells is asymmetrical, with a spike during austral spring in both  $H_s$  and  $T_p$  (Fig.

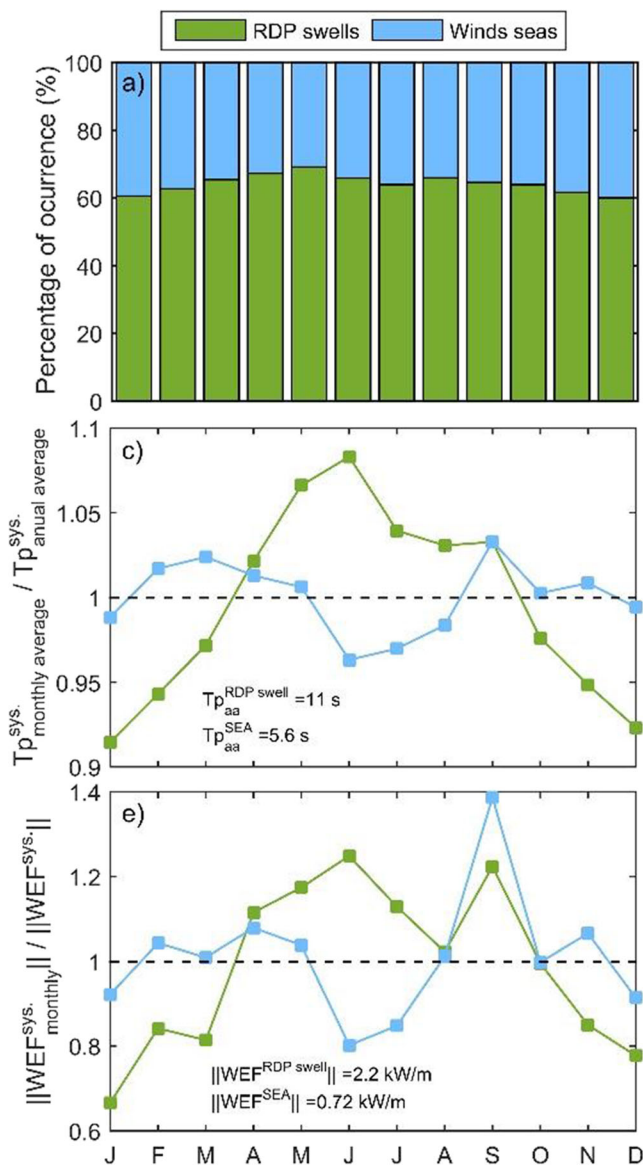
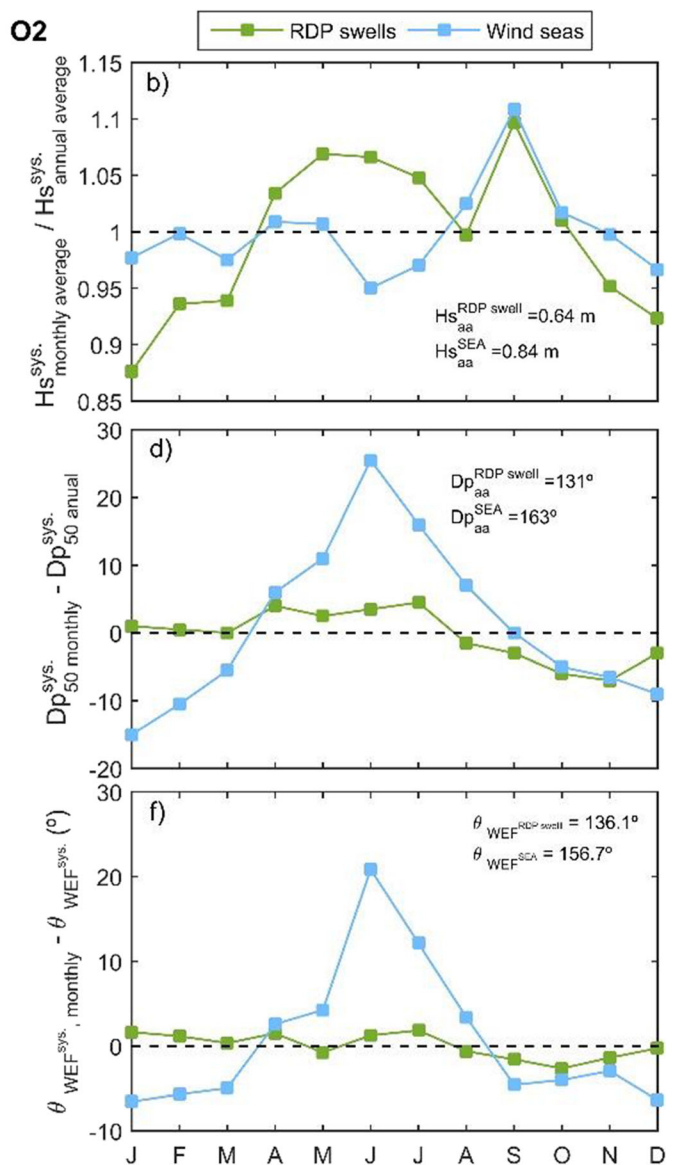


**Fig. 28** Annual cycles of different wave systems parameters at O2. **a** Frequency of occurrence, **b**  $H_s$ , **c**  $T_p$ , **d**  $D_p$ , **e** magnitude of the mean wave energy flux, and **f** direction of the mean wave energy flux

27b and c); this in turn affects the annual cycle of the WEF that during these months show a counterclockwise rotation (Fig. 10). Moreover, September is an atypical month, with a clear spike in the energy of both wind seas and southern, eastern, and RDP swells (Figs. 27, 28, and 29), resulting in a clear peak in total  $H_s$  (Fig. 6). Lastly, there is a decrease in the wave energy during winter at some locations in the RDP particularly in June (Fig. 6) that is produced by a clockwise rotation of the wind (and wind seas; Figs. 28 and 29), with winds coming from the SW quadrant, resulting in a reduced fetch.

The difference between the Atlantic and the RDP coast is also evident from the inter-annual variability.



The  $H_s$ ,  $T_{m01}$ , and  $||WEF||$   $COV_{annual}$  are larger in the RDP than in the Atlantic, while the annual  $Dm_{75-25}$  is larger in the Atlantic than in the RDP (Figs. 7 and 11). When looking at the time series of mean (or median) annual parameters (Figs. 8 and 12), two features stand out: first, a cycle of roughly 20 years for  $T_{m01}$  in the Atlantic and outer RDP; secondly, a positive trend for both wave and WEF directions (a clockwise rotation). The former is attributable to the southern swells (Fig. 30a), while the latter comes from a trend in the direction of wind seas (Fig. 30b, d, and e).

The delimitation of the ocean areas where the two swell systems are generated (Fig. 31a and b) shows that

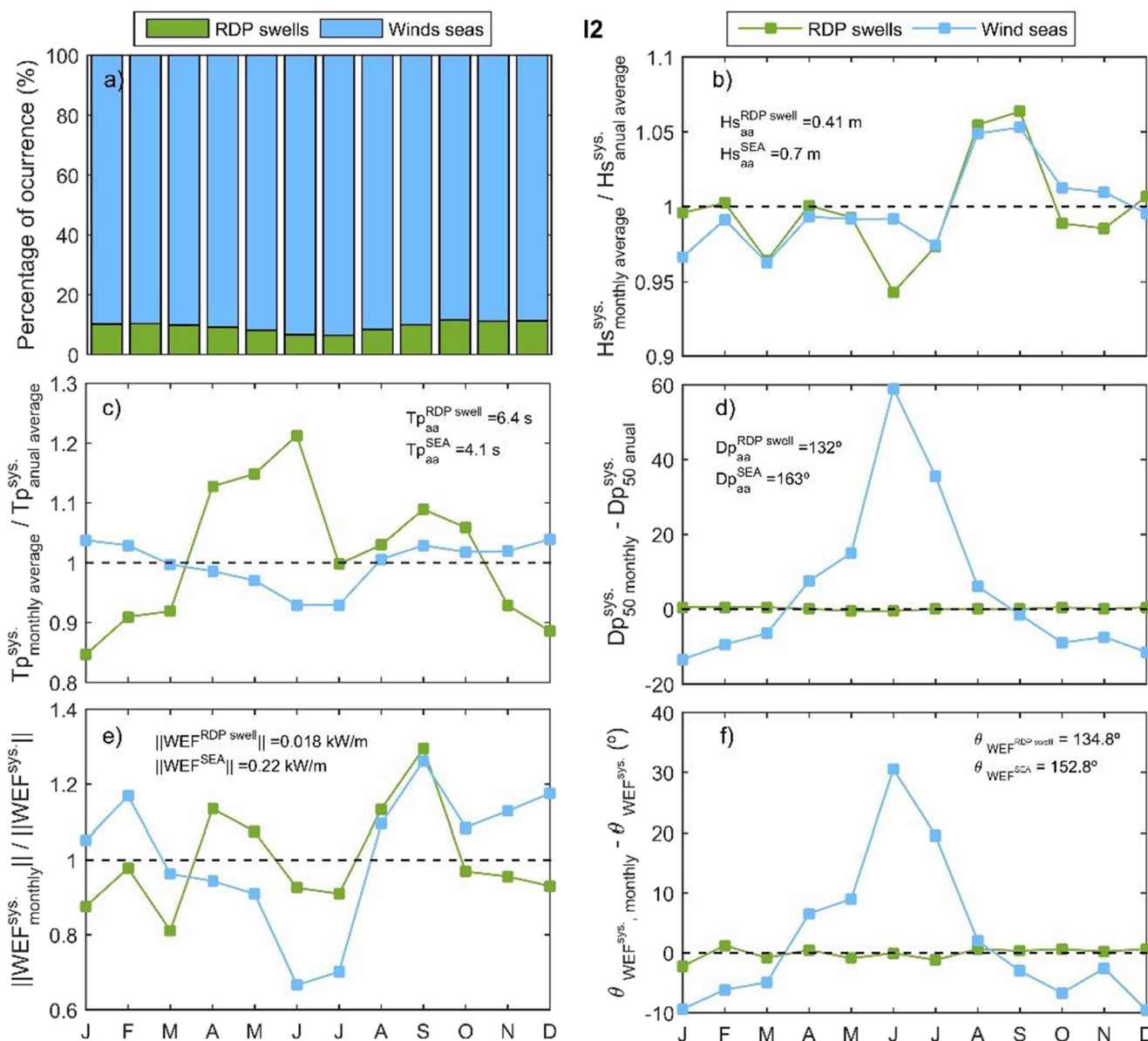


**Fig. 29** Annual cycles of different wave systems parameters at I2. **a** Frequency of occurrence, **b**  $H_s$ , **c**  $T_p$ , **d**  $D_p$ , **e** magnitude of the mean wave energy flux, and **f** direction of the mean wave energy flux

larger correlation values are found for locations relatively close to the Uruguayan coast, somehow explaining the similarity between wind seas and swells climate observed in the Atlantic (Fig. 23). On the other hand, the area of highest correlation with the Southern swells is further away from the Uruguayan coast than that of the eastern swells, resulting in southern swells having larger wave periods (Fig. 21). Moreover, the area of high correlation is larger for southern swells than for eastern swells and encompasses latitudes of high storminess. Conversely, the area of high correlation of the eastern swell falls within the influence zone of the South Atlantic semi-permanent

high (Sun et al. 2017), in agreement with results showing southern swells being more energetic than eastern swells (Fig. 25).

Lastly, from the analysis of the climate indexes (Table 2), it results that the climate index with the largest correlation with the wave climate in the Uruguayan coast is the Antarctic Oscillation index (AAO), in agreement with previous results presented in Alonso et al. (2015), and also with results from studies performed at a larger scale (Stopa et al. 2013; Marshall et al. 2018). Its correlation with the two swell systems have opposite signs, positive with the eastern swells and negative with



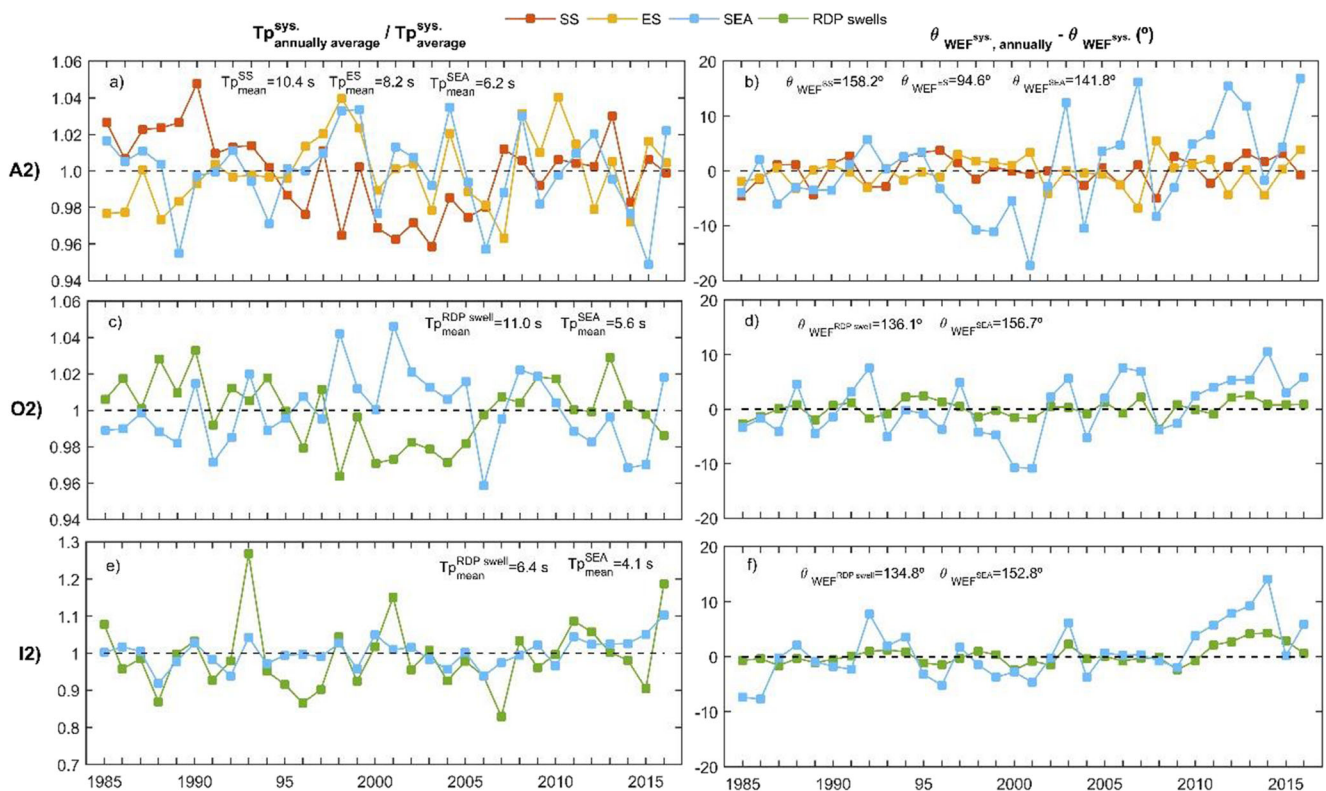


**Fig. 30** Inter-annual variation of different wave systems **a**  $T_p$  at node A2, **b** direction of the mean wave energy flux ( $\theta_{\text{WEF}}^{\text{sys}}$ ) at A2, **c**  $T_p$  at O2, **d**  $\theta_{\text{WEF}}^{\text{sys}}$  at O2, **e**  $T_p$  at I2, and **f**  $\theta_{\text{WEF}}^{\text{sys}}$  at I2

the southern swells; as both systems contribute to the RDP swells, the opposite correlations appear to neutralize each other, and no significant correlation is found between AAO and RDP swells. Regarding wind seas, the correlation with AAO is significant and positive for the entire coast. The separation between LTWS allowed perceiving more clearly the influence of the AAO, which would have been largely hidden if only correlation with  $H_s$  (i.e., integral parameter) had been analyzed, as can be seen in Stopa et al. (2013) and Reguero et al. (2015). Regarding SOI, no significant correlation was found with any LTWS.

### 5 Conclusions

A combination, and when necessary the adaptation, of a series of tools originally proposed for off-shore and/or deep water conditions was used for a regional characterization of the coastal wave climate, showing a way forward to take advantage of the increasingly frequent high-resolution wave hindcasts and of the information contained in the wave spectra. In particular, it was shown that the combination of Hanson and Phillips

(2001) method to separate swells and wind seas with the long-term wave system approach of Portilla-Yandún et al. (2015) is modified to include an ad hoc posterior re-grouping step that considered the orientation of the coast, and allowed to define wave systems that were coherently identified all along the coast. Also, it is showed that using LTWS allows to unmask and better interpret some regional patterns and processes, as well as their relationship with global atmospheric processes, that otherwise would be hidden. This approach allows analyzing and interpreting the wave climate in an environment that gradually transitions from open waters to a semi-enclosed sea; something so far little studied and that could be applied in similar environments around the world.

Regarding our case study, although the analysis considers from the first moment the usual division of the Uruguayan coast into Atlantic, Outer RDP, and intermediate and inner RDP, the obtained results sustain this regionalization in terms of wave climate, providing the distinctive characteristics of each region for the first time. In the Atlantic coast, the change is driven mainly by changes on coastal orientation, where La Paloma was identified as a breaking point, while in the RDP, the effect of the bathymetry and the geometry of the estuary (fetches) play a

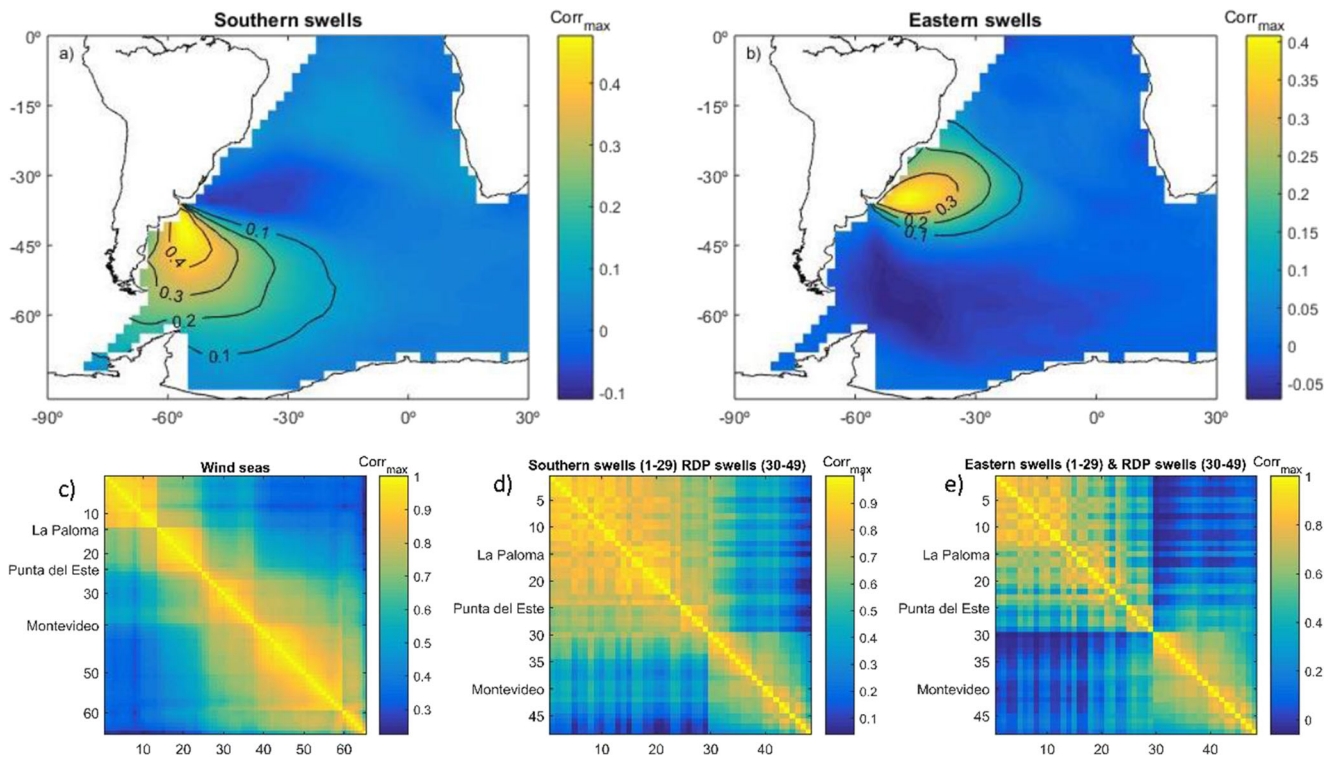


**Fig. 31** Maximum correlation (i.e., maximum absolute value of the linear correlation that is obtained between two time series by varying the time lag between them) between **a** Hs of the southern swells and wind projection on the azimuth, **b** Hs of eastern swells and wind projection on the azimuth, **c** Hs of Wind seas at different nodes, **d** Hs of Eastern swells prolonged with RDP swells at different nodes, and **e** Hs of Southern swells prolonged with RDP swells at different nodes. The

axes of **c**, **d**, and **e** correspond to the analyzed nodes identified with numbers. Being the eastern more nodes the one and numbering from this to west (see Fig. 1). La Paloma (Node #15), Punta del Este (Node #25), and Montevideo (Node #35) are included to provide geographic references. The diagrams corresponding to swells (**b** and **c**) are limited to the node #49 because west to this node swells is insignificant (see Fig. 26c)

major role, with a noticeable difference between annual cycles of  $H_s$  and WEF to the east and to the west of Montevideo. A common feature observed in the wave climate all along the coast is a peak in wave energy ( $H_s$  and WEF) during September, with contributions from all LTWS. In terms of inter-annual variability, it was found that AAO is the climate index that most affects wave climate in the area and that there exist a trend to

clockwise rotation of the WEF, something that could have profound impacts on coastal morphology.

Lastly, the distinction between wave systems used here might be useful to improve wave modeling in the study area, as it would facilitate assessing the performance of the model separating by wave systems, allowing the identification of specific problems of each one and guiding future met-ocean research in the region.

**Table 2** Linear correlation between monthly mean Hs per system and climate indexes. An average of the Atlantic nodes (1-25) was considered for the eastern and southern swells, an average of nodes 30 to 49 was considered for RDP swells, and average of the nodes indicated in the

names were considered for wind seas. Only those correlations statistically significant at 90 % are shown. The correlations statistically significant at 95% are highlighted in bold

	Eastern swell	Southern swell	RDP swell	Wind seas 1–14	Wind seas 15–25	Wind seas 26–38	Wind seas 39–49
AAO	<b>0.14</b>	<b>-0.18</b>	-	<b>0.16</b>	<b>0.10</b>	<b>0.11</b>	<b>0.11</b>
SOI	-	-	-	-	-	-	-

**Supplementary Information** The online version contains supplementary material available at <https://doi.org/10.1007/s10236-021-01469-6>.

**Funding** This work was partially funded by the Uruguayan Agency for Research and Innovation (ANII) through its “Fondo María Viñas” program, contract number FMV\_3\_2016\_1\_125918, and by the United Nations Development Programme project “URU/18/002 Integración del enfoque de adaptación en ciudades, infraestructura y ordenamiento territorial”. Rodrigo Alonso acknowledges the financial support provided by ANII through the postgraduate scholarships program, grant number POS-NAC-2012-1-8936.

## References

- Almar R, Kestenare E, Reynolds J, Jouanno J, Anthony EJ, Laibi R, Hemer M, du Penhoat Y, Ranasinghe R (2015) Response of the Bight of Benin ( Gulf of Guinea , West Africa ) coastline to anthropogenic and natural forcing , Part1 : Wave climate variability and impacts on the longshore sediment transport. *Cont Shelf Res* 110:48–59. <https://doi.org/10.1016/j.csr.2015.09.020>
- Alonso R, Solari S (2020) Improvement of the high-resolution wave hindcast of the Uruguayan waters focusing on the Río de la Plata Estuary. *Coast Eng* 161:103724. <https://doi.org/10.1016/j.coastaleng.2020.103724>
- Alonso R, Solari S, Teixeira L (2015) Wave energy resource assessment in Uruguay. *Energy* 93:683–696. <https://doi.org/10.1016/j.energy.2015.08.114>
- Amante C, Eakins BW (2009) ETOPO1 1 arc-minute global relief model: procedures, data sources and analysis. In: NOAA Technical Memorandum NESDIS NGDC-24. NOAA, National Geophysical Data Center. <https://doi.org/10.7289/V5C8276M>
- Ardhuin F, Rogers E, Babanin A, Filipot J-F, Magne R, Roland A et al (2009) Semi-empirical dissipation source functions for ocean waves: Part I, definition, calibration and validation. *J Phys Oceanogr* 40(9):1917–1941. <https://doi.org/10.1175/2010JPO4324.1>
- Campos RM, Alves JHGM, Guedes Soares C, Guimaraes LG, Parente CE (2018) Extreme wind-wave modeling and analysis in the South Atlantic Ocean. *Ocean Model* 124(August 2017):75–93. <https://doi.org/10.1016/j.ocemod.2018.02.002>
- Campos RM, Soares CG, Alves JHGM, Parente CE, Guimaraes LG (2019) Regional long-term extreme wave analysis using hindcast data from the South Atlantic Ocean. *Ocean Eng* 179(March):202–212. <https://doi.org/10.1016/j.oceaneng.2019.03.023>
- Chawla A, Spindler DM, Tolman HL (2013) Validation of a thirty year wave hindcast using the Climate Forecast System Reanalysis winds. *Ocean Model* 70:189–206. <https://doi.org/10.1016/j.ocemod.2012.07.005>
- Chowdhury P, Ranjan M (2017) Progress in Oceanography Effect of long-term wave climate variability on longshore sediment transport along regional coastlines. *Prog Oceanogr* 156:145–153. <https://doi.org/10.1016/j.pocean.2017.06.001>
- Collins M, Cai W, Ganachaud A, Guilyardi E, Jin F, Jochum M et al (2010) The impact of global warming on the tropical Pacific Ocean and El Niño. *Nat Geosci* 3:391–397. <https://doi.org/10.1038/ngeo868>
- De Oliveira MMF, Ebecken NFF, De Oliveira JLF, Gilleland E (2011) Generalized extreme wind speed distributions in South America over the Atlantic Ocean region. *Theor Appl Climatol* 2:377–385. <https://doi.org/10.1007/s00704-010-0350-3>
- Dragani WC, Romero SI (2004) Impact of a possible local wind change on the wave climate in the upper Río de la Plata. *Int J Climatol* 24(9):1149–1157. <https://doi.org/10.1002/joc.1049>
- Elshinnawy AI, Medina R, Gonzalez M (2017) On the relation between the direction of the wave energy flux and the orientation of equilibrium beaches. *Coast Eng* 127:20–36. <https://doi.org/10.1016/j.coastaleng.2017.06.009>
- Gong D, Wang S (1999) Definition of Antarctic oscillation index. *Geophys Res Lett* 26(4):459–462
- Gramscianinov CB, Hodges KI, Camargo R (2019) The properties and genesis environments of South Atlantic cyclones. *Clim Dyn* 53(7):4115–4140. <https://doi.org/10.1007/s00382-019-04778-1>
- Gramscianinov CB, Campos RM, Soares CG, Camargo RD (2020) Extreme waves generated by cyclonic winds in the western portion of the South Atlantic Ocean. *Ocean Eng* 213(April):107745. <https://doi.org/10.1016/j.oceaneng.2020.107745>
- Hanson JL, Phillips OM (2001) Automated analysis of ocean surface directional wave spectra. *J Atmos Ocean Technol* 18(2):277–293. [https://doi.org/10.1175/1520-0426\(2001\)018<0277:AAOOSD>2.0.CO;2](https://doi.org/10.1175/1520-0426(2001)018<0277:AAOOSD>2.0.CO;2)
- Hervouet J-M (2007) Hydrodynamics of free surface flows: modelling with the finite element method. Jhon Willey & Sons Ltd., Chichester, UK, p 360
- Jiang H, Mu L (2019) Wave Climate from spectra and its connections with local and remote wind climate. *J Phys Oceanogr* 49:543–559. <https://doi.org/10.1175/JPO-D-18-0149.1>
- Marshall GJ (2003) Trends in the southern annular mode from observations and reanalyses. *J Clim* 16:4134–4143
- Marshall AG, Hemer MA, Hendon HH, McInnes KL (2018) Southern annular mode impacts on global ocean surface waves. *Ocean Model* 129(July):58–74. <https://doi.org/10.1016/j.ocemod.2018.07.007>
- Martín-Gómez V, Barreiro M, Mohino E (2020) Southern hemisphere sensitivity to ENSO Patterns and Intensities: impacts over subtropical South America. 11(77). 11. <https://doi.org/10.3390/atmos11010077>
- Menstachi L, Vousdoukas M I, Voukouvalas E, Dosoia A, Feyen L (2017) Global changes of extreme coastal wave energy fluxes triggered by intensified teleconnection patterns. *Geophys Res Lett* 44:2416–2426. <https://doi.org/10.1002/2016GL072488>
- Meyer F (1994) Topographic distance and watershed lines. *Signal Process* 38:113–125
- Pereira HPP, Violante-Carvalho N, Nogueira ICM, Babanin A, Liu Q, de Pinho UF, Parente CE (2017) Wave observations from an array of directional buoys over the southern Brazilian coast. *Ocean Dyn* 67(12):1577–1591. <https://doi.org/10.1007/s10236-017-1113-9>
- Pianca C, Mazzini PLF, Siegle E (2010) Brazilian offshore wave climate based on NWW3 reanalysis. *Braz J Oceanogr* 58(1):53–70. <https://doi.org/10.1590/S1679-87592010000100006>
- Pisciottano G, Díaz A, Cazes G, Mechoso CR (1994) El Niño–Southern Oscillation impact on rainfall in Uruguay. *J Clim* 7:1286–1302
- Portilla-Yandún J, Cavaleri L, Ph G, Vledder V (2015) Ocean Surface Waves Wave spectra partitioning and long term statistical distribution. *Ocean Model* 96:148–160. <https://doi.org/10.1016/j.ocemod.2015.06.008>
- Portilla-Yandún J, Barbariol F, Benetazzo A, Cavaleri L (2019) On the statistical analysis of ocean wave directional spectra. *Ocean Eng* 189(August):106361. <https://doi.org/10.1016/j.oceaneng.2019.106361>
- Quefférou P, Croizé-Fillon DJ (2013) Global altimetry SWH Data Set. IFREMER Internal Technical Report
- Reguero BG, Losada IJ, Méndez FJ (2015) A global wave power resource and its seasonal, interannual and long-term variability. *Appl Energy* 148:366–380. <https://doi.org/10.1016/j.apenergy.2015.03.114>
- Rodrigues RR, Campos EJD, Haarsma R (2015) The Impact of ENSO on the South Atlantic Subtropical Dipole Mode. *J Clim* 28(7):2691–2706. <https://doi.org/10.1175/JCLI-D-14-00483.1>
- Romeu MAR, Fontoura JAS, Melo E (2015) Typical scenarios of wave regimes off Rio Grande do Sul, Southern Brazil. *J Coast Res*



- 299(1998):61–68. <https://doi.org/10.2112/JCOASTRES-D-12-00085.1>
- Saha S, Moorthi S, Pan HL, Wu X, Wang J, Nadiga S, Tripp P, Kistler R, Woollen J, Behringer D, Liu H, Stokes D, Grumbine R, Gayno G, Wang J, Hou YT, Chuang HY, Juang HMH, Sela J, Iredell M, Treadon R, Kleist D, van Delst P, Keyser D, Derber J, Ek M, Meng J, Wei H, Yang R, Lord S, van den Dool H, Kumar A, Wang W, Long C, Chelliah M, Xue Y, Huang B, Schemm JK, Ebisuzaki W, Lin R, Xie P, Chen M, Zhou S, Higgins W, Zou CZ, Liu Q, Chen Y, Han Y, Cucurull L, Reynolds RW, Rutledge G, Goldberg M (2010) The NCEP climate forecast system reanalysis. *Bull Am Meteorol Soc* 91(8):1015–1057. <https://doi.org/10.1175/2010BAMS3001.1>
- Saha S, Moorthi S, Wu X, Wang J, Nadiga S, Tripp P, Behringer D, Hou YT, Chuang HY, Iredell M, Ek M, Meng J, Yang R, Mendez MP, van den Dool H, Zhang Q, Wang W, Chen M, Becker E (2014) The NCEP climate forecast system version 2. *J Clim* 27(6):2185–2208. <https://doi.org/10.1175/JCLI-D-12-00823.1>
- Santoro P, Fossati M, Tassi P, Huybrechts N, Pham D, Bang V, Piedra-cueva JCI (2017) A coupled wave – current – sediment transport model for an estuarine system : Application to the Río de la Plata and Montevideo Bay. *Appl Math Model* 52:107–130. <https://doi.org/10.1016/j.apm.2017.07.004>
- Shimura T, Mori N (2019) High-resolution wave climate hindcast around Japan and its spectral representation. *Coast Eng* 151:1–9. <https://doi.org/10.1016/j.coastaleng.2019.04.013>
- Solari S, Alonso R, Teixeira L (2018) Analysis of coastal vulnerability along the Uruguayan coasts. *J Coast Res* 85:1536–1540. <https://doi.org/10.2112/SI85-308.1>
- Splinter KD, Davidson MA, Golshani A, Tomlinson R (2012) Climate controls on longshore sediment transport. *Cont Shelf Res* 48:146–156. <https://doi.org/10.1016/j.csr.2012.07.018>
- Stopa JE, Fai K, Tolman HL, Chawla A (2013) Patterns and cycles in the Climate Forecast System Reanalysis wind and wave data. *Ocean Model* 70:207–220. <https://doi.org/10.1016/j.ocemod.2012.10.005>
- Stopa JE, Ardhuin F, Babanin A, Zieger S (2016) Comparison and validation of physical wave parameterizations in spectral wave models. *Ocean Model* 103(July):2–17. <https://doi.org/10.1016/j.ocemod.2015.09.003>
- Sun X, Cook KH, Vizy EK (2017) The South Atlantic subtropical high: climatology and interannual variability. *Clim Dyn* 30:3279–3296. <https://doi.org/10.1175/JCLI-D-16-0705.1>
- Teixeira L, Piedra-Cueva I, Solari S (2012) The influence of fluvial and maritime processes in shaping the eastern coast of the upper Rio de la Plata estuary. *River Flow 2012 - Proceedings of the International Conference on Fluvial Hydraulics* Vo. 1 pp. 813-820. ISBN: 978-146657551-6
- The WAVEWATCH III® Development Group (WW3DG) (2016) User manual and system documentation of WAVEWATCH III® version 5.16. Tech. Note 329, NOAA/NWS/NCEP/MMAB, College Park, MD, USA, 326 pp. + Appendices
- The WAVEWATCH III® Development Group (WW3DG) (2019) User manual and system documentation of WAVEWATCH III® version 6.07. Tech. Note 333, NOAA/NWS/NCEP/MMAB, College Park, MD, USA, 326 pp. + Appendices
- Tolman HL (2008) A mosaic approach to wind wave modeling. *Ocean Model* 25(1–2):35–47. <https://doi.org/10.1016/j.ocemod.2008.06.005>
- Walker GT, Bliss EW (1932) *World Weather V*. *Memoirs of the Royal Meteorological Society* 4(36):53–83
- Walker GT, Bliss EW (1937) *World Weather VI*. *Memoirs of the Royal Meteorological Society* 4(39):119–139